論文 / 著書情報
Article / Book Information

題目(和文)	結晶中の単一希土類イオンの低温分光測定
Title(English)	Spectroscopy of a single rare-earth ion in a crystal at cryogenic temperature
著者(和文)	中村一平
Author(English)	Ippei Nakamura
出典(和文)	学位:博士（理学）, 学位授与機関:東京工業大学, 報告番号:甲第9708号, 授与年月日:2015年3月26日, 学位の種別:課程博士, 審査員:松下　道雄,奥田　雄一,上妻　幹旺,村上　修一,旭　耕一郎,細谷　暁夫
Citation(English)	Degree:, Conferring organization: Tokyo Institute of Technology, Report number:甲第9708号, Conferred date:2015/3/26, Degree Type:Course doctor, Examiner:,,,,,
学位種別(和文)	博士論文
Type(English)	Doctoral Thesis

Ph.D. thesis

Spectroscopy of a single rare-earth ion in a crystal at cryogenic temperature

Ippei Nakamura

Tokyo Institute of Technology

February 19th, 2015

Preface

Centuries after ancient Greek philosophers pondered over the conceptual idea of atom to explain the universe, the concept of atom revived in France to establish stoichiometry. Nowadays, atoms and molecules are no longer conceptual ideas but their existence is a solid fact. Real atoms and molecules drive scientists to observe and to control behavior of individual atoms and molecules. Observation of photo-activity of a single quantum system in condensed media, so-called single-molecule spectroscopy, has initiated in 1989. Today, the single-molecule spectroscopy has enormous significance in the context of quantum information technologies, where the observation and the control of a quantum system are inseparable from each other.

This thesis describes the single-ion spectroscopy of Rare-Earth (RE) ion doped in crystal. When cooled down to a few kelvins, the nuclear spin transition of RE ions doped in a crystal is known to be detected using its optical transition. RE ions have forbidden optical transitions between two $4f$ electronic configurations with a long radiation lifetime reaching to 100 μs. The hyperfine splitting about 10 MHz due to the nuclear spin appears on the spectral line of the ions, whose linewidth narrows down to 10 kHz of its lifetime-limited width at a few K. Aiming at the optical detection and manipulation of a single RE nuclear spin quantum state, the author has consulted on the low-temperature spectroscopy of single praseodymium ions doped in a lanthanum trifluoride crystal (Pr^{3+}:LaF_3).

Spectroscopy of a single Pr^{3+} requires the sensitivity enough to detect the weak luminescence due to the long radiation lifetime and the frequency resolution close to the narrow spectral linewidth of the ion. Thus, the author needed to build the cryogenic confocal microscope dedicated to carry out the single-ion spectroscopy of Pr^{3+}:LaF_3. A high performance objective for the cryogenic microscopy was newly developed with the numerical aperture of 0.97 and the detection efficiency of the confocal setup was as large as 0.48%. The excitation lightsource consists of a commercial continuous-wave diode laser and an optical Fabry-Perot cavity as the stable laser frequency reference. The laser linewidth was made narrower than

0.4 MHz and the long-time stability of the output frequency was ±0.018 MHz/day.

Photo-luminescence excitation measurement of individual Pr^{3+} ions was demonstrated with a bulk crystal of 0.05% Pr^{3+}-doped LaF_3 cooled down at 1.5 K. Spectral lines of the ${}^3H_4 \rightarrow {}^3P_0$ transition of individual Pr^{3+} ions were resolved as luminescence peaks with intensities of $20 - 30$ cps and the full-width at half-maximum of approximately 3 MHz at an excitation intensity of 80 W cm^{-2}. The population transfer of a single Pr nuclear spin was demonstrated via the optical pumping process of the ion.

This study is the first success of the single-RE spectroscopy with a bulk crystal sample which contains multiple RE ions in the microscopic volume. It benefits future implementation of multi-qubit operations based on the ion-ion interaction to address the individual ions close in the sub-micrometer distance by the inhomogeneous distribution of their transition frequency. In application to nuclear spin qubit, qubit manipulation is conducted under the magnetic field to use Zeeman sub-levels. Because the Zeeman effect is anisotropic, the orientation of the magnetic field must be accurately controlled with respect to the host crystal. The experiment using the bulk crystal sample paves the way for the optical access to a single ion under the Zeeman field. The author believes this study established the first step to utilizing the RE-doped crystal as the solid-state quantum-information processor.

This thesis is organized into five chapters. Chapter 1 introduces the significance and also the difficulty of the spectroscopy of single RE ions doped in a crystal. Chapter 2 covers physical and chemical properties of the sample material Pr^{3+}:LaF_3 and the spectroscopic method to resolve individual Pr^{3+} ions abundantly contained in the bulk crystal sample. Chapter 3 describes the development of the home-build cryogenic confocal setup to carry out the single-ion spectroscopy. Chapter 4 includes the results of the photo-luminescence excitation spectroscopy of Pr^{3+}:LaF_3 at 1.5 K and the discussion about the success of the single-Pr^{3+} detection and origins of observed spectral widths of individual ions. Chapter 5 summarizes the entire study and declares the outlook of quantum information processing using a RE-doped bulk crystal.

Contents

Chapter 1

Introduction

The atom and molecule is the smallest building block of chemical materials. All macroscopic physical or chemical phenomenons express the integration of microscopic actions of the Avogadro number of such tiny particles. In the field of material sciences, observations of a single atom or molecule is the manifest capstone of sensitivity. Obviously, the poor signal makes the experiments extremely difficult. In the last few decades, *single-molecule spectroscopy*, observation of the photo-activity of single quantum emitter (such as atoms, molecules, quantum-dots, color centers), has been initiated.

Pioneering works of single-atom spectroscopy were made with the atomic beam and the ion trap techniques. In 1977, Kimble, Dagenais, and Mandel demonstrated the anti-bunching measurement of Na atoms in the atomic beam, but the complete anti-bunching signal did not appear due to the fluctuation of the atom number of the beam and the limited interaction time between the light and the flying atoms [1]. Once the observation of a very few number of atoms was succeeded by the ion trap [2], trapping of a single atom was naturally tried. The non-classical behavior of photons emitted by a single atom was confirmed by the anti-bunching measurement of a trapped Mg^+ ion by Diedrich and Walther [3]. Following the atomic beam and the ion trap, the next trial of single-atom observation was the spectroscopy of a single ion doped in a crystal. The experiment using an emitter captured in a solid promises the arbitrary interaction time and the measurement without the Doppler broadening. The first report was the optical detection of dilute Sm^{2+} ions doped in a bulk CaF_2 crystal performed by Lange, Grill, and Martienssen [4]. They tried to resolve individual Sm^{2+} ions distributed dispersedly in the crystal, however, the result was limited to the detection of the Poisson-like fluctuation of a very few number of the ions contained in the microscopic volume.

The first success of the single-molecule detection in solid is reported by Moerner and Kador in 1989 [5]. The absorption spectrum of a single pentacene was taken by the frequency-modulation Stark double modulation spectroscopy of a pentacene-doped *p*-terphenyl crystal at 1.6 K. The essence of their experiment is that the narrow homogeneous width and the wide inhomogeneous width of the pentacene molecules was employed to resolve a specific one molecule from the others. *Homogeneous width* is the absorption linewidth which individual emitters are expected to exhibit. The transition wavelength of emitters doped in a solid shows the distribution called *inhomogeneous width*, which is given by the inhomogeneity of local environments surrounding each emitters. In the case of materials like pentacene-doped *p*-terphenyl, the homogeneous width becomes much narrower than the inhomogeneous width when phonons dissipate at a few kelvins. A part of pentacene molecules in the detection volume can be observed selectively by tuning the wavelength of a lightsource to a specific position of the inhomogeneously broadened absorption spectrum. They achieved to detect a single pentacene molecule whose spectral line was isolated from other molecules at the wing of the inhomogeneously broadened spectrum.

Not only to spectrally resolve a single molecule from the bulk, in the first place, the narrow spectral line is to be the origin of abundant spectroscopic information harvested by the single-molecule spectroscopy. The energy of photons absorbed and emitted by a single quantum emitter corresponds to the energy gap between the two quantum states before and after the transition. The sharpness of the spectral line defines the resolution of the energy structure of the emitter, which can be revealed by spectroscopic measurements.

The optical detection of a single spin is an especially significant fruit of the high-resolution spectroscopy of a single quantum emitter. The flip of a single electron or nuclear spin produces an electro-magnetic signal with an energy of at most $h \times 1$ GHz while a photon has the energy over $h \times 100$ THz in the visible wavelength region. If the quantum state of a spin can be transcribed to that of an emitted photon, the signal is to be amplified over five orders of magnitude. In addition to its high brilliance, the optical single-spin detection has been extensively subjected with an aim to constitute the quantum information interface between flying photons and localized spin qubits for the large scale quantum information transfer, processing and storage. The spin-detection method depends on each systems. Kohler *et al.* and Wrachtrup *et al.* independently conducted the Optically Detected Magnetic Resonance (ODMR) of the excited spin triplet state of a single pentacene molecule by detecting the modulation of the photo-emitting rate [6, 7]. Wrachtrup *et al.* demonstrated the optical read-out and manipulation of a single electron spin of a Ce^{3+} ion [8]. Their experiment stands on the

selection rule of circular polarized light. For single quantum emitters whose homogeneous width is narrower than the fine structure of the electronic ground state, the spin state can be distinguished by measuring the transition frequency. Such the spectroscopic single-spin detection has been applied to optical systems such as Nitrogen-Vacancy (NV) defect center in diamond [9, 10].

Rare-Earth (RE) ions doped in crystal concurrently allows the spectroscopic detection of the nuclear spin and the spectral addressing of individual RE ions. At a few kelvins, the homogeneous width of the transitions between $4f$ electronic states narrows down to the order of 10 kHz and 10 MHz of the hyperfine structure appears on the absorption spectra. The nuclear spin transition of ensemble RE ions has been observed by ODMR [11] and the Raman-heterodyne detection of the opto-magnetic double resonance [12,13]. Also the optical manipulation of the spins has been conducted by the optical pulse sequence e.g. Stimulated-Raman Adiabatic Passage (STIRAP) [14]. The inhomogeneous width about 1-10 GHz [15] enables the frequency selection of a specific subset of ions which occupy the same spectral position in the bulk absorption spectrum. Quantum information processing including the two features of RE-doped crystal are proposed by Kroll *et al*. as Rare-Earth Quantum Computer (REQC) [16] and by Ichimura as Frequency-domain quantum computer [17]. In these schemes, RE ions are classified into a cluster sharing the same optical transition frequency and the nuclear spins of each ionic clusters are individually observed and manipulated as an ensemble spin qubits by the frequency-tuned light. The introductory experiments have already been demonstrated [18–20].

The ultimate picture of the RE quantum information processor is to address single RE ions by their transition frequency and make them into the integrated single-spin qubits. However, the observation of a single RE ion is inevitably hampered by its weak optical activity. In general, the homogeneous width is inversely proportional to both the radiation lifetime of the excited state and the spontaneous emission rate. This constraint results in that the excitation of a narrower spectral line produces the weaker photo-luminescence. To enforce the high resolution spectroscopy and to reduce an amount of emitters to the single atom level make the luminescence signal fatally small. The radiation lifetime of Mg^+ ion observed by the single-ion trap [3] was only 4 ns. In contrast, that of Sm^{2+} ion used in ref. [4] is as long as 2 μs and some radiative transition of RE ions have a long lifetime reaching to 100 μs. The spectroscopy of transition-metal ions in crystal is the third candidate of the single-atom spectroscopy following the atomic beam and the ion trap, however, it had been foiled just because of the weak luminescence of transition ions.

At the dawn of the 2000s, the single-ion detection was demonstrated by using RE-doped nanocrystal or the thin-doped layer sample [21–23]. An advantage of these sample morphology is the low background emission from other RE ions in the sample. Especially the nanocrystal sample can be prepared to which contains only a single RE ion by the optimization of particle size and doping stoichiometry. The microscopy of a single RE-doped particle readily arrives at the observation of a single RE ion. In 2003, Malyukin *et al.* performed the time-correlated single photon counting (TCSPC) of a single Pr^{3+} doped Y_2SiO_5 nanoparticle and proved such particle can be utilized as a single photon source [23].

However, these experiments faced the limit that single RE ions were not resolved spectrally but only spatially by the conventional microscopic setup. The lack of spectral addressing depending on the large inhomogeneous distribution undermine the motivation to conduct the single RE detection bearing with the grossly weak luminescence. To execute the two-qubit operations mentioned in the REQC scheme, the two ions need to get close within a distance of 100 nm to yield the interaction between two RE ions [16]. By considering that the spatial resolution of the standard optical microscope never exceeds 100 nm in the visible wavelength region, the sufficient interaction depth probably does not arise between the ions displaced from each other over the microscopic resolution. For this reason, further advanced experiments have required the spectral addressing of individual RE ions in the microscopic volume and the luminescence detection technique robust to the background signal from the other ions densely doped in the entire sample.

Attempts to circumvent the weak luminescence of RE ion have been progressed rapidly in the past few years. One of the methods to circumvent the weak emission of the ion is to convert photo-emission into a different photo-physical event for easier detection. Kolesov *et al.* detects the up-conversion luminescence from the $5d$ state of a single Pr^{3+} ion doped in a Y_2SiO_5 nanocrystal at room temperature [24]. Goto *et al.* fabricated a Pr^{3+}-doped Y_2SiO_5 crystal itself into the Fabry-Perot optical cavity and meditates the observation of coupling between the cavity-enhanced light field and a single Pr^{3+} ion in the crystal [25]. Yin *et al.* succeeded to detect photo-ionization of a single Er^{3+} ion using a Single Electron Transistor (SET) [26]. Approximately 30-40 Er^{3+} ions were spectrally addressed, and the fine structure of the absorption spectrum of the single ion, which is affected by both a electron spin and a Er nuclear spin, was resolved. To improve the efficiency of photo-luminescence detection is also a promising approach. Utikal *et al.* conducted the microspectroscopy of a Pr^{3+}-doped Y_2SiO_5 nanocrystal using a solid immersion technique [27]. The low background emission of nanocrystal sample and the high photon-collection efficiency of the solid immersion lens

enabled them to spectrally address multiple Pr^{3+} ions in the nanocrystal. Even the state preparation of a single Pr nuclear spin was demonstrated by using the optical pumping process of the ion.

While the trials of the single-RE spectroscopy have been continued, also the author and members of Matsushita group have consulted on the low temperature spectroscopy of a single RE ion doped in a bulk inorganic crystal over 7 years. The sample is a 0.05% Pr^{3+}-doped bulk LaF_3 crystal cooled down to 1.5 K by superfluid helium. There are mainly two purposes to adopt such a highly-doped bulk sample. The one is the high-concentration of Pr^{3+} ion. The number density of Pr^{3+} is 10^7 μm^{-3}, that is, 10^4 of Pr^{3+} ions are contained in a microscopic volume of approximately $(100\ nm)^3$. As the similar experiment was conducted for pentacene in *p*-terphenyl, we aim to spectrally resolve individual Pr^{3+} ions at the wing of the inhomogeneously-broadened absorption spectrum. The other purpose is to apply an static magnetic field in the future. In application to nuclear spin qubit, qubit manipulation is conducted under the magnetic field to use Zeeman sub-levels. Because the Zeeman effect is anisotropic, the magnetic field must be applied along a well-controlled direction with respect to the host crystal. If optical detection of a single ion is established for a bulk crystal, optical access to a single ion under the Zeeman field will be readily attained.

The photo-luminescence detection of Pr^{3+} is conducted by exciting the ${}^3H_4 \rightarrow {}^3P_0$ transition, which is a well-studied transition between the two $4f^2$ electronic states of Pr^{3+} [28]. Once the single-ion detection is achieved, experiments made on a bulk sample such as spectral hole-burning driven by optical pumping of nuclear spin population can be readily downscaled to a single-ion level. Needless to add, the poor signal and the intensive background emission stand up against the experiment without all benefits of novel samples and excitation/detection methods employed in other studies. Our approach is to develop a high numerical aperture (NA) objective that works at a few K. A larger solid-angle of collection and a smaller focal volume of the objective makes our setup sensitive enough to detect a single Pr^{3+} ion in a bulk crystal.

The single-ion spectroscopy was carried by a home build cryogenic setup. To resolve the narrow absorption line of a single Pr^{3+}, the linewidth of the lightsource was made narrower than 0.4 MHz. The confocal reflecting microscope had the detection efficiency up to 0.43%. Spectral lines of the ${}^3H_4 \rightarrow {}^3P_0$ transition of individual Pr^{3+} ions were resolved as luminescence peaks with intensities of $20 - 30$ cps and the full-width at half-maximum of approximately 3 MHz at an excitation intensity of 80 W cm^{-2}. The population transfer of a single Pr nuclear spin was demonstrated via the optical pumping process of the ion.

Chapter 2

Spectroscopy of a single Pr^{3+} ion in a LaF_3 crystal

2.1 Electronic states and optical transitions of Pr^{3+}:LaF_3

Rare-Earth (RE) element is a general term of elements including Yttrium (Y), Scandium (Sc) and 15 elements called *lanthanoid*. Lanthanoid is an element group whose atomic numbers range from 57 (La) to 71 (Lu). Trivalent cations of lanthanoid (Ln^{3+}) are chromatic, and these elements are widely used to dye for grasses or ceramics, graze of potteries, phosphor, and lasing media [29].

The electron configuration of Ln^{3+} is [Xe] $4f^n$, where n is the number of $4f$ electrons. The $4f$ orbitals of Ln^{3+} ions are partially occupied except La^{3+} ($n = 0$) and Lu^{3+} ($n = 14$). These $4f$ electrons carry the optical-activity of Ln^{3+} in the visible and the Near InfraRed (NIR) region. These electrons are shielded from environmental perturbation by an outer closed shell of $5s$ and $5p$ orbitals. Thus, $4f - 4f$ optical transitions of Ln^{3+} have a long coherence lifetime and a narrow homogeneous width. In solid, the oscillation strength of a transition between $4f^n$ states is at most the order of 10^{-7}. This value is much smaller than the oscillation strength of a typical allowed transition (order of 0.1) because the $4f^n$ transition is primarily forbidden due to the violation of the angular momentum conservation. The weak interaction with the host matrix enables such forbidden transitions marginally.

Praseodymium (Pr) is a rare-earth element whose atomic number is 59 and atomic mass is 140.9. The trivalent cation Pr^{3+} takes on a green color in crystal or solution. The electron configuration of Pr^{3+} is [Xe] $4f^2$. The electronic states are indexed by the Russell-Saunders

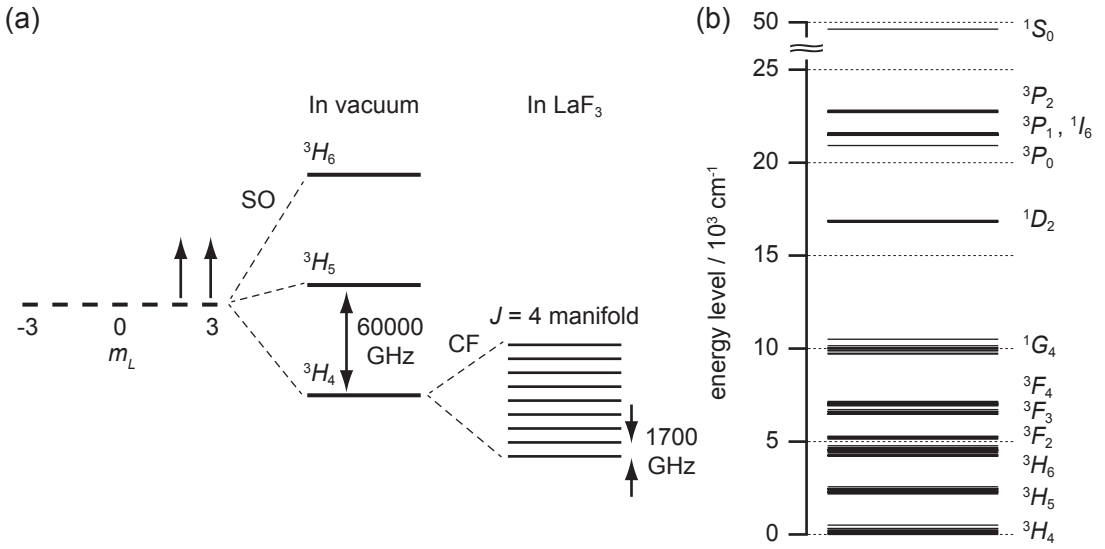

Figure 2.1 $4f^2$ Electronic states of Pr^{3+} in a crystal. (a) Splitting structure of the electronic ground state. Abbreviations are m_L: magnetic quantum number; SO: Spin-Orbital coupling; CF: Crystal Field. This figure is prepared by consulting ref. [30]. (b) Energy levels of Pr^{3+}:LaF_3. The energy is represented in 10^3 cm^{-1} $\approx$ 30000 GHz. This diagram was made from the experimental data investigated by Caspers *et al.* [31].

term symbol $^{2S+1}L_J$, where L is the total orbital angular momentum quantum number, S is the total spin angular momentum quantum number, and J is the total angular momentum quantum number of orbital and spin. In the case of the $4f^2$ configuration, L ranges from 0 to 6 (corresponding terms are from S to I) and S takes values of 0 or 1. For each combination of (L, S), J ranges from $|L - S|$ to $|L + S|$. Figure 2.1a shows the ground-state energy structure of Pr^{3+}. Determined from Hund's rules, the most stable state is the ^3H, which means that the spin triplet and the maximal L are simultaneously realized. The spin-orbital interaction disparts the $^3H_{J=4-6}$ states and the lowest is the $^3H_4$. When Pr^{3+} is doped in a crystal, each $^{(2S+1)}L_J$ state splits into maximally $(2J + 1)$ sublevels due to the low-symmetry crystal field. The splitting width between the $J = 4$ manifold of the $^3H_4$ state is approximately 1000 GHz. In the case of LaF_3, the splitting between the lowest manifold of the $^3H_4$ and the second lowest is 1700 GHz. At 1.5 K ($k_BT \approx 50$ GHz), Pr^{3+} ions are no longer excited thermally and the all ions occupy the lowest manifold of the $^3H_4$ state. Only the transitions from this state will appear on the absorption spectrum. Figure 2.1 displays the all $4f^2$ electronic states of Pr^{3+}:LaF_3 including the ground $^3H_4$ state.

The $^1D_2$ and $^3P_0$ states are well-investigated emissive states of Pr^{3+}:LaF_3 [28]. The radiative lifetimes (T_1) are respectively 520 μs and 47 μs [32]. In our work, observation of single

Pr^{3+} was carried by detecting the photo-luminescence from the $^3P_0$ state because the shorter lifetime brings the spontaneous emission rate one order of magnitude larger. The radiative deactivation processes from the $^3P_0$ state are roughly divided into the two cases, the direct transition to the ground state ($^3H_4$) and the transitions to the intermediate electronic states including the $^3H_6$ state. The latter is suitable for photo-luminescence detection because it is easy to separate the red-shifted emission from the excitation light by long-wavelength pass filters. Figure 2.2 shows the emission spectrum of the $^3P_0$ state of Pr^{3+}:LaF_3. Transmittances of two long-wavelength pass filters used in our home-build microscope are also displayed in the figure.

The maximum luminescence rate of single Pr^{3+} can be estimated as follows. From the spontaneous emission rate of the $^3P_0$ state ($1/T_1 = 2.1 \times 10^4$ s^{-1}) and the luminescence quantum yield of the $^3P_0$ state (0.63 from ref. [32]), the maximum number of luminescence photons emitted from a single Pr^{3+} is calculated to be 1.3×10^4 s^{-1}. Among the radiative deactivation processes from $^3P_0$, the probability of emission at a wavelength longer than 530 nm, which is the cut-off wavelength of the long-wavelength-pass filter (BI-0019, Semrock), is calculated from ref. [33] to be 0.52. Thus, the maximum number of photons passing through the filter is

$$\begin{aligned} \Gamma &= 0.52 \cdot 2.1 \times 10^4 \text{ s}^{-1} \\ &= 7.0 \times 10^3 \text{ s}^{-1}. \end{aligned} \tag{2.1}$$

Γ was used to evaluate the luminescence signal intensity of a single Pr^{3+} in section 3.2.

2.2 Hyperfine structure of the $^3H_4 \rightarrow {}^3P_0$ transition

Energy levels of Pr^{3+} show the hyperfine structure due to Pr nuclear spin ($I = 5/2$). Figure 2.3 shows the electronic ground and excited states and their hyperfine structure [11, 34, 35]. Both the ground $^3H_4$ and the excited $^3P_0$ states split into three sublevels due to show the pseudo quadrupole interaction between the nuclear spin and the electric filed gradient (EFG) given by the electrons. For the $^3H_4$ state, the energies of the three hyperfine sublevels with respect to the lowest are 0, 16.7, and 25.2 MHz. For the $^3P_0$ state, only the two adjacent splittings are known to be 0.7 and 1.1 MHz. The optical absorption of the lowest $^3H_4$ to the $^3P_0$ transition appears at a wavelength of $\nu_0 = 627.33$ THz ($\lambda_0 = 477.89$ nm). At a few kelvins, the homogeneous width of the $^3H_4 \rightarrow {}^3P_0$ transition narrows down to the order of 10 kHz, which is limited by the radiative lifetime of the excited $^3P_0$ state $T_1 = 47$ μs. In such a

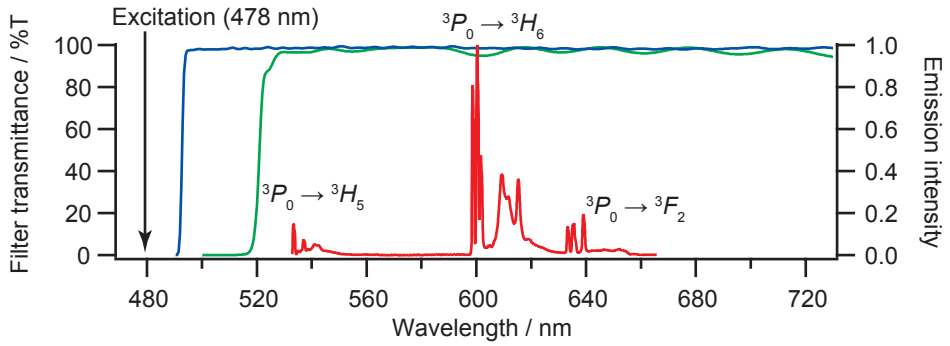

Figure 2.2 Emission spectrum of Pr^{3+}:LaF_3 at 1.5 K. The excitation wavelength was set to 478 nm to excite the $^3H_4 \rightarrow {}^3P_0$ transition. The red curve is the emission spectrum (right axis). Emission peaks of the $^3P_0 \rightarrow {}^3F_{3,4}$ and $^1G_4$ transitions are out of the range of the spectrometer. The blue curve and green curve is the transmittance of long-wavelength-pass filters LP488-RS25 (Semrock) and BI0019 (Semrock) respectively (left axis).

condition, the nuclear quadrupole splitting appears as a resolved structure of the absorption spectrum.

2.3 Host crystal

The crystal structure of LaF_3 is *tysonite* structure, which is the typical trigonal structure of LnF_3 including PrF_3 [12,37,38]. The space group of the crystal is $p\bar{3}c1$. LaF_3 crystal is clear and colorless in the visible region because the electron configuration of La^{3+} closes at [Xe], and La^{3+} does not have $4f$ electrons unlike other Ln^{3+}. The refractive index of LaF_3, was investigated by Laiho and Lakkisto [39].

$$n_{\mathrm{O}} = \sqrt{1 + \frac{\lambda^2}{0.6505 \cdot \lambda^2 - 5.044 \times 10^{-15}}} \tag{2.2}$$

$$n_{\mathrm{EO}} = \sqrt{1 + \frac{\lambda^2}{0.6600 \cdot \lambda^2 - 5.093 \times 10^{-15}}} \tag{2.3}$$

where λ [m] is the wavelength of an incident light. n_{O} is the value for *ordinarily ray*, whose polarization is perpendicular to the c-axis of LaF_3. n_{EO} is the value for *extraordinarily ray*, whose polarization is parallel to the c-axis. The approximate value at the visible region ($\lambda = 400 - 700$ nm) is $n = 1.6$.

Figure 2.4 shows La cites in LaF_3 crystal. The cite symmetry of La cite is C_2 because La cites place on two fold symmetry axes lying on the c-axial plane. There are 6 La cites in the parallelogram-pole shaped unit cell whose lattice constants are $a = 0.7185$ nm for the a-axis

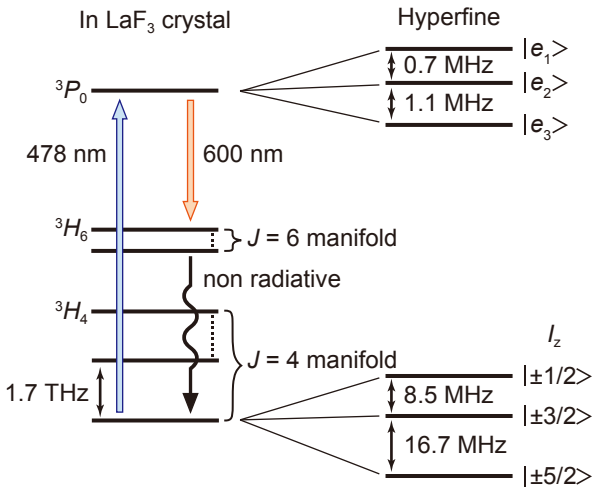

Figure 2.3 Electronic states and hyperfine structure of Pr^{3+}:LaF_3. The nine-fold degeneracy of the ground $^3H_4$ state is lifted in LaF_3 by the crystal field of C_2 symmetry. Both the ground $^3H_4$ and the excited $^3P_0$ states split to three to show the hyperfine structure due to Pr nuclear spin ($I = 5/2$). For the $^3H_4$ state, energy of the three hyperfine sublevels with respect to the lowest is 0, 16.7, and 25.2 MHz. For the $^3P_0$ state only the two adjacent splittings are known to be 0.7 and 1.1 MHz. This figure is prepared from the journal article of our group [36] (I. Nakamura *et al.*, *Scientific Reports* **4**, 7364, 2014).

and $c = 0.7351$ nm for the c-axis. The number density of La cite is

$$\frac{6}{a^2 \sin 120^\circ \cdot c} = 1.828 \times 10^{10}\ \mu\mathrm{m}^{-3}. \tag{2.4}$$

The sample used in our work is a 0.05% Pr^{3+}-doped LaF_3 crystal. The size of the crystal is $4 \times 5 \times 6$ mm^3. The c-axial plane was polished for optical measurements. Because Pr^{3+} ions substitute 0.05% of La^{3+} ions in the crystal, the number density of Pr^{3+} is

$$5 \times 10^{-4} \cdot 1.828 \times 10^{10}\ \mu\mathrm{m}^{-3} = 9.140 \times 10^{6}\ \mu\mathrm{m}^{-3}. \tag{2.5}$$

2.4 Optical detection of individual Pr^{3+} ions in bulk crystal

As it is clear from the number density, the sample crystal contains numerous Pr^{3+} ions. To resolve the signal of only a single Pr^{3+} ion, both the microscopic and the spectroscopic selection were employed. Figure 2.5a shows the schematic of the essential part of the microscopic setup. The excitation light is focused on the sample to illuminate only a microscopic volume intensively. The microscope objective employed in our work has the focal-spot with the radius of $r_{\mathrm{HM}} = 0.11$ μm and the focal depth of $z_{\mathrm{HM}} = 1.2$ μm (detailed in subsection 3.1.2).

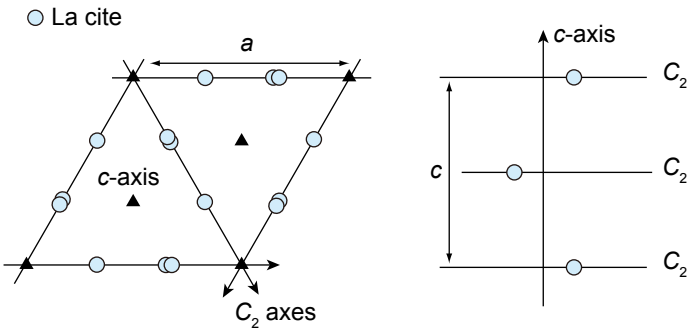

Figure 2.4 Distribution of La cites in LaF_3. (left) Viewing the c-axial plane. (right) Viewing the $c - C_2$ axial plane.

The focal volume is roughly evaluated to be $\pi r_{\mathrm{HM}}^2 \cdot z_{\mathrm{HM}} = 4.6 \times 10^{-2}\ \mu\mathrm{m}^3$. The number of Pr^{3+} ions contained in the focus is calculated from the focal volume and the number density (2.5).

$$4.6 \times 10^{-2}\ \mu\mathrm{m}^3 \cdot 9.140 \times 10^{6}\ \mu\mathrm{m}^{-3} = 4.2 \times 10^{5}. \tag{2.6}$$

Four hundred-thousand of Pr^{3+} ions still remain in the objective focus. The inhomogeneous broadening of the optical absorption frequency was utilized to resolve a single Pr^{3+} ion from other ions. Figure 2.5b represents the schematic of the ${}^3H_4 \rightarrow {}^3P_0$ transition of Pr^{3+}:LaF_3. Pr^{3+} ions doped in the sample form the inhomogeneously broadened absorption spectrum whose inhomogeneity originates from the local strain of the crystal [15]. The spectrum is a Lorentzian-like shape whose FWHM is 12.7 GHz (detailed in subsection 4.1.2). When the sample was illuminated by an excitation laser whose linewidth is much narrower than the inhomogeneous width, only a limited number of Pr^{3+} ions absorb the laser light. Tuning the our home-build lightsource (0.4 MHz linewidth) to the center of the absorption spectrum ν_0, a fraction of excited ions is roughly evaluated to be the ratio of the laser linewidth and the inhomogeneous width 0.4 MHz/12.7 GHz $= 3 \times 10^{-5}$. Thus, the number of excited ions n_0 is to be

$$\begin{aligned} n_0 &= 4.2 \times 10^{5} \cdot 3 \times 10^{-5} \\ &\approx 10. \end{aligned} \tag{2.7}$$

When the excitation frequency is detuned from ν_0, the number of excited ions gets fewer. Assuming the Lorentzian shape, the number of excited ions is described as

$$n(\Delta\nu) = \frac{n_0}{1 + \Delta\nu^2/\Gamma_{\mathrm{inh}}^2}, \tag{2.8}$$

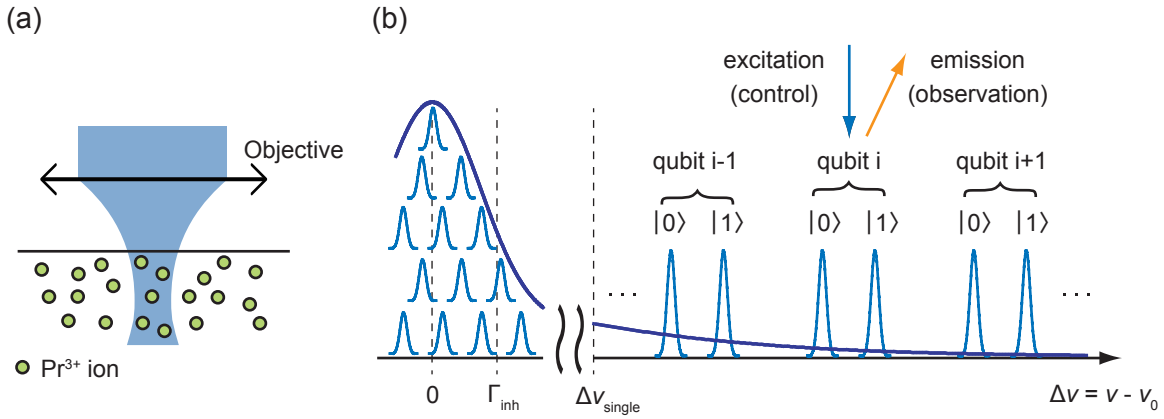

Figure 2.5 Spatial and spectral selection of a single Pr^{3+} ion doped in a bulk crystal. (a) Essential part of the microscopic setup. (b) The ${}^3H_4 \rightarrow {}^3P_0$ transition of Pr^{3+}:LaF_3. The deep blue curve represents the inhomogeneously broadened absorption spectrum of the transition. The pale blue curves represent absorption of individual Pr^{3+} ions in the objective focus. The horizontal axis is the detuning from the center frequency $\nu_0 = 627.33$ THz ($\lambda_0 = 477.89$ nm).

where $\Delta\nu$ is the detuning of the laser frequency from ν_0 and Γ_{inh} is the inhomogeneous width represented in the half-width at half-maximum. If $n(\Delta\nu)$ decreases to $< 1/10$, spectral lines of individual ions can be resolved as isolated peaks [5]. Such detuning range $\Delta\nu_{\text{single}}$ satisfies the relation below.

$$\frac{n_0}{1 + \Delta\nu_{\text{single}}^2/\Gamma_{\text{inh}}^2} = \frac{1}{10}. \tag{2.9}$$

Solving the equation for $\Delta\nu_{\text{single}}$,

$$\Delta\nu_{\text{single}} = \sqrt{10n_0 - 1}\,\Gamma_{\text{inh}}. \tag{2.10}$$

Substituting $n_0 = 10$ and $\Gamma_{\text{inh}} = 12.7/2$ GHz to (2.10),

$$\Delta\nu_{\text{single}} \approx 60 \text{ GHz}. \tag{2.11}$$

We aim to observe the photo-luminescence excitation spectrum of a single Pr^{3+} ion isolated at the wing of inhomogeneously broadened absorption where $\Delta\nu > \Delta\nu_{\text{single}}$. The final objective of our work is to conduct the spectral addressing of individual Pr^{3+} ions in a bulk crystal and the optical detection and control of Pr nuclear spin qubits.

Chapter 3

Experimental setup

3.1 Objective

3.1.1 Single-piece reflecting objective

Objective lens is the essential component which determines the spatial resolution and the sensitivity of optical microscope. Performance benchmark of objective is a value called Numerical Aperture (NA).

$$\mathrm{NA} = n \sin\theta, \tag{3.1}$$

where n is a refractive index of a matrix filling a space between an objective and a sample and θ is half of an angular aperture of the objective (Fig. 3.1). The light spot focused on the focal plane has the width comparable with its wavelength λ. The spot radius of an ideal (aberration-free) lens is known as the Airy Disk radius r_{A}.

$$r_{\mathrm{A}} = 0.61 \frac{\lambda}{\mathrm{NA}}. \tag{3.2}$$

The solid angle of collection for an emitter at the focus is described as below.

$$\begin{aligned} \Omega &= \int_0^{2\pi} \mathrm{d}\phi \int_0^{\theta} \sin\theta \mathrm{d}\theta \\ &= 2\pi(1 - \cos\theta), \end{aligned} \tag{3.3}$$

where ϕ is the azimuthal angle around optical axis (z) and its contribution appears only as a coefficient value of 2π when the lens was made axially symmetric.

High performance objectives which has NA close to $\sin 90^\circ = 1$ are commercially supplied. However, such objectives could not be used with the low-temperature spectroscopic

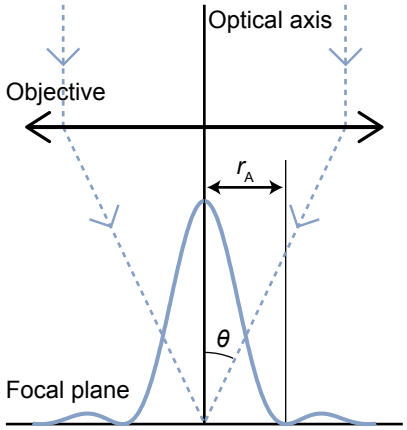

Figure 3.1 Parallel rays pass through the objective and the focused spot on the focal plane. θ is an angle between the optical axis and the refracted rays which pass through the outer edge of the incident aperture of the lens. The Airy disk radius r_A is the radius of the First Dark Ring (FDR, the first local minimum from the center) of the spot focused by the ideal lens.

setup, because these objectives consist of multiple lenses and do not work normally in liquid helium due to the misalignment of the lenses accompanying with the mechanical distortion. Thus, an objective used in liquid helium needs to be a singlet. There has been a study using an aspherical singlet (NA = 0.55) for the low-temperature spectroscopy of a single molecule in the Near-InfraRed (NIR) region [40], although the chromatic aberration makes it impossible to employ singlets to the luminescence spectroscopy in the visible region where dispersion of refractive index becomes larger than the NIR region.

Figure 3.2 shows the single-piece reflecting objectives developed in our group. These objectives focus the incident beam or collimates emission from the focal point by convex and concave aluminum mirrors fabricated on a single-piece of fused-silica. Robust optical alignment of the objective in superfluid helium is guaranteed by the singlet design and the reflecting design eliminates chromatic aberration. Figure 3.2 left is the conventional single-piece reflecting objective (SRO) with two spherical mirrors (NA = 0.58) [41]. The single-molecule detection in visible region has been performed by using this objective [42]. However, the SRO lacks the sensitivity to detect a single RE ion, whose emission rate is lower about three orders of magnitude than that of organic dye molecules. The spherical aberration of spherical mirrors makes NA of the SRO lower than commercial high-NA objectives. As discussed by Fujiwara and coauthors, further improvement of NA (> 0.6) deteriorates focusing ability because the spherical aberration simultaneously increased with the angular aperture [43]. To overcome the spherical aberration, Inagawa *et al.* designed an single-piece aspheric reflect-

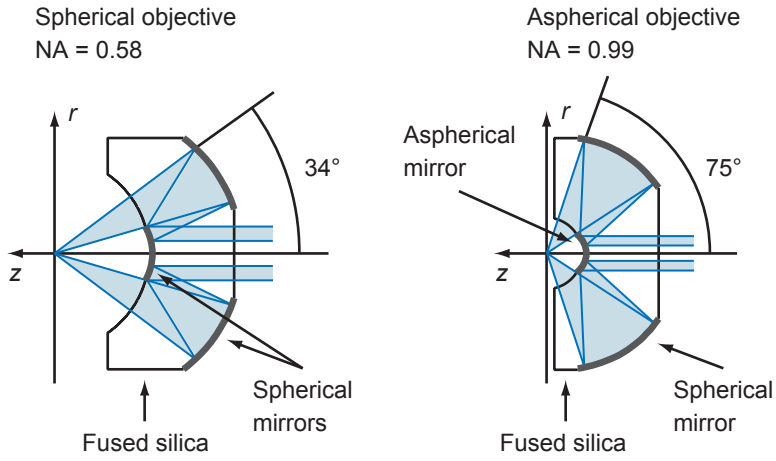

Figure 3.2 Two designs of single-component reflecting objective developed in our group for optical measurement of a point emitter in superfluid helium. (left) Low-NA objective consisting of two spherical mirrors. (right) High-NA objective consisting of one aspherical convex and one spherical concave mirrors.

ing objective (ARO, Fig. 3.2b) [44]. The convex mirror was made aspherical to cancel the spherical aberration of the spherical concave mirror. The NA value of the ARO reached to 0.99, almost the maximal value in superfluid helium, i.e., $n_{\mathrm{He}} \sin(90°) = 1.03$, where n_{He} is the refractive index of superfluid helium [45]. Two AROs has been manufactured by Sankyo Optics Industry yet. Single Pr^{3+} spectroscopy was performed by the second piece of ARO (No. 2), which was delivered in May 2012.

The collection solid angle of a single-piece reflecting objective is calculated as below.

$$\begin{aligned} \Omega &= \int_0^{2\pi} \mathrm{d}\phi \int_{\theta_{\min}}^{\theta_{\max}} \sin\theta \mathrm{d}\theta \\ &= 2\pi(\cos\theta_{\min} - \cos\theta_{\max}), \end{aligned} \tag{3.4}$$

where $\theta_{\max}$ is half of the angular aperture of the concave mirror and $\theta_{\min}$ is the minimum angle at which rays are not blocked by the aspherical convex mirror (Fig. 3.3a). For the emitter placed in a high refractive-index matrix (like RE ions doped in a crystal), the effective angular aperture decreases due to the refraction at the interface (Fig. 3.3b). There is a relation known as Snell's law (3.5) between incident and refraction angles of rays (θ and θ') at the

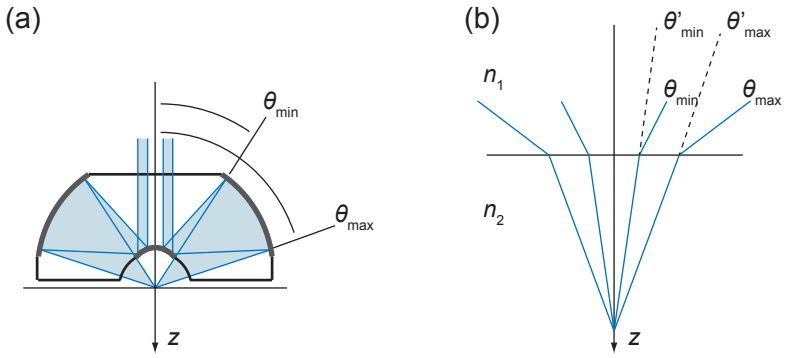

Figure 3.3 Definition of incident angles of rays for single-piece reflecting objectives. All incident angles in the figure are measured from the optical axis of the objective (z). (a) Homogeneous medium (vacuum, air and so on). (b) Two mediums contact at the flat surface.

interface of two matrices (refractive indices, n_1 and n_2).

$$n_2 \sin\theta' = n_1 \sin\theta, \tag{3.5}$$

$$\cos\theta' = \sqrt{1 - \left(\frac{n_1}{n_2}\right)^2 \sin^2\theta}. \tag{3.6}$$

Including the effect of refraction ($\theta_{\mathrm{max,min}} \rightarrow \theta'_{\mathrm{max,min}}$), the solid angle of collection (3.4) is modified as below.

$$\Omega = 2\pi(\cos\theta'_{\mathrm{min}} - \cos\theta'_{\mathrm{max}}) \tag{3.7}$$

$$= 2\pi\left(\sqrt{1 - \left(\frac{n_1}{n_2}\right)^2 \sin^2\theta_{\mathrm{min}}} - \sqrt{1 - \left(\frac{n_1}{n_2}\right)^2 \sin^2\theta_{\mathrm{max}}}\right). \tag{3.8}$$

The interesting situation here is that emitters are doped in a LaF_3 crystal and the space between the crystal and the objective is filled by superfluid helium ($n_{LaF_3}/n_{He} = 1.56$ [39,45]). Tables 3.1 and 3.2 show $\theta_{\mathrm{min,max}}$ and Ω of two single-piece reflecting objectives for homogeneous matrices and the LaF_3 crystal immersed in superfluid helium. The solid angle of the ARO is four times larger than that of the SRO for emitters in a homogeneous matrix and even three times larger for emitters doped in LaF_3 crystal immersed in superfluid helium.

3.1.2 Performance of the aspheric reflecting objective

The spatial resolution and the collection efficiency of the ARO (No. 2) were evaluated by the objective pair method using a commercial high-NA objective (MPLAPON50X, $f = 3.60$mm, NA $= 0.95$, Olympus) as a reference (Fig. 2.6). The incident parallel beam was focused by

Table. 3.1 Angular aperture and solid angle of the spherical reflecting objective.

matrix	$\theta_{\max}$	$\theta_{\min}$	Ω	$\Omega/4\pi$
homogeneous	34.2°	16.2°	0.27π	0.067
superfluid / LaF_3	21.1°	10.3°	0.10π	0.025

Table. 3.2 Angular aperture and solid angle of the aspherical reflecting objective.

matrix	$\theta_{\max}$	$\theta_{\min}$	Ω	$\Omega/4\pi$
homogeneous	74.8°	32.9°	1.16π	0.289
superfluid / LaF_3	38.2°	20.3°	0.30π	0.076

the ARO and collimated by the reference objective. A plano-convex lens (f = 450 mm) focused the collimated beam on a CMOS image sensor. The focused spot at the focal plane of the ARO was magnified on the CMOS imaging plane with the magnification ratio equal to the ratio of the focal length of two lenses $\frac{450\text{ mm}}{3.60\text{ mm}} = 125\times$. Distance between the objectives can be scanned by driving the z-stage actuator on which the reference objective was mounted. Thus, the spatial resolution along the optical axis could also be investigated.

Quality of the focused spot of the objective pair never exceeds that of the reference objective. The performance of MPLAPON50X was needed to be evaluated before testing the ARO. Thus, the focused spot of MPLAPON50X was taken with MPLAPON100X (f = 1.80 mm, NA = 0.95, Olympus), which has the same NA value as MPLAPON50X and is expected to show the same or better performance. Figure 3.5a is the focused spot of the two commercial objectives. Figure 3.5b is the one-dimensional spot made from (a). The intensity of each CMOS pixel is plotted versus the distance of the pixel from the center of the spot (x, y = 0 μm). The intensity curve drops almost perfectly to zero at the Airy disk radius $r_{\mathrm{A}} = 0.61\frac{\lambda}{\mathrm{NA}} = 300$ nm, where λ = 473 nm and NA = 0.95. The resolution along the optical axis (z) was shown in Fig. 3.5c. This curve is the plot of the total intensity gathered in the circle with the radius of r_{A} versus the distance between two objectives (z position). The curve has the FWHM of 1.4 μm. These results are to be compared with the results of the ARO.

Figure 3.6 shows the focused image and the focal depth of the objective pair of the ARO (No. 2) and MPLAPON50X. Figure 3.6a is the focused spot taken at a wavelength of 473 nm. In comparison with the image of the commercial objective pair (Fig. 3.5), the concentric rings in the image are more clearly visible. This is because the aspheric convex mirror shields a part of the incident beam and obstructs the entrance pupil of the objective. The red curve

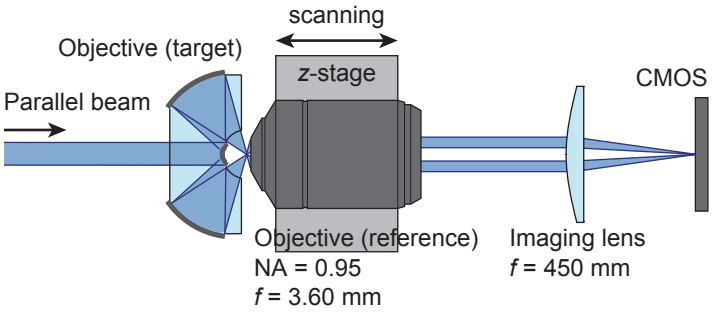

Figure 3.4 Setup to evaluate the ARO by the objective pair method.

in Fig. 3.6b is the one-dimensional spot made from (a). The radius of the FDR was $r_{\mathrm{FDR}} = 250$ nm. r_{FDR} is slightly smaller than $r_{\mathrm{A}} = 300$ nm. The ARO showed the spatial resolution commensurate with its NA value in the focal plane. The blue curve shows the Encircled Energy (EE) of the ARO. EE(r) is the ratio of the total energy (intensity) gathered in the circle with a radius of r to that of the entire spot. EE(r_{FDR}) = 24% is an important benchmark to evaluate the light-collection efficiency of the ARO. It corresponds to the net fraction of the excitation light gathered in the objective focus or the emission collected by the ARO. EE of the ARO will be used to estimate the excitation density (subsection 3.1.3) and the detection efficiency (subsection 3.2.2) of the confocal setup. Figure 3.6c shows the resolution along the optical axis (z). The blue curve is the plot of the total intensity gathered in r_{FDR} (250 nm) versus the distance between two objectives. The focal depth was 1.2 μm in FWHM. The red curve is the z-profile of the commercial objective pair (reproduction of the curve in Fig. 3.5c). The result that the focal depth of the ARO (1.2 μm) is shallower than that of the reference objectives (1.4 μm) means that the ARO shows better spatial resolution than the reference objective. It turned out that the spatial resolution of the ARO could not be evaluated accurately by the objective pair methods. Paradoxically, the performance of the ARO seems too excellent.

A more accurate evaluation which does not need the reference objective is being conducted by Inagawa and coworkers (Inagawa *et al.*, *in preparation* [44]). Performance of the ARO was evaluated from a fluorescence images of five single quantum dots (Qdot 705 ITK Carboxyl, Invitrogen) taken by newly developed 3D sample scanning system at 1.5 K. With excitation at 532 nm, the fluorescing spot had the widths in the focal plane of $\Gamma_{x,y} = 0.212 \pm 0.008$ μm and that along the optical axis of $\Gamma_z = 0.91 \pm 0.04$ μm in FWHM. Γ_z is smaller than the focal depth of the objective pair with MPLAPON50X (1.2 μm in FWHM). This fact confirms that the focal depth of the reference objective set the lower limit of the objective pair in Fig. 3.6c.

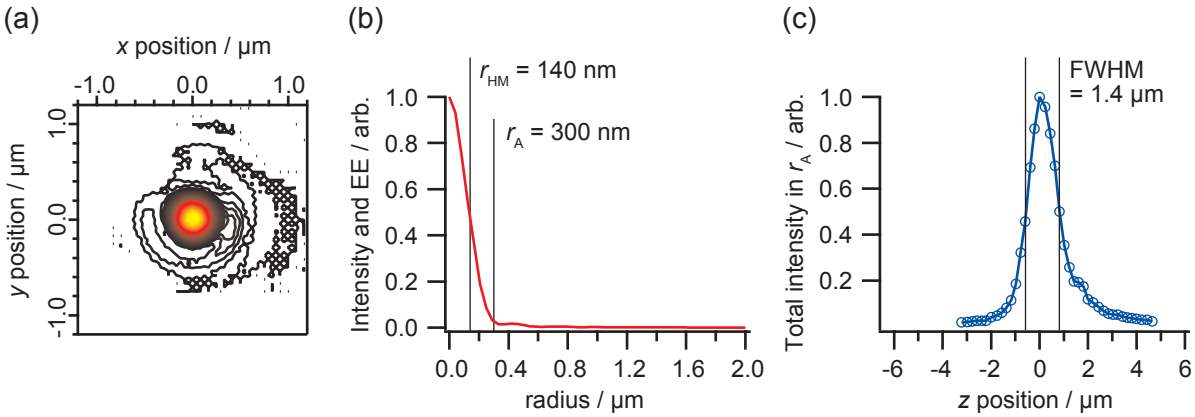

Figure 3.5 Focused spot and spatial resolution of the commercial high-NA objective pair. (a) Focused spot taken by the CMOS camera (λ = 473 nm). x and y positions are the scale at the focal plane of the tested objective. (b) One-dimensional spot. (c) Resolution along the optical axis. Integrated intensity in r_A = 300 nm was plotted versus distance between the two objectives (z). z = 0 is set to the distance where the best focused image (a) was taken.

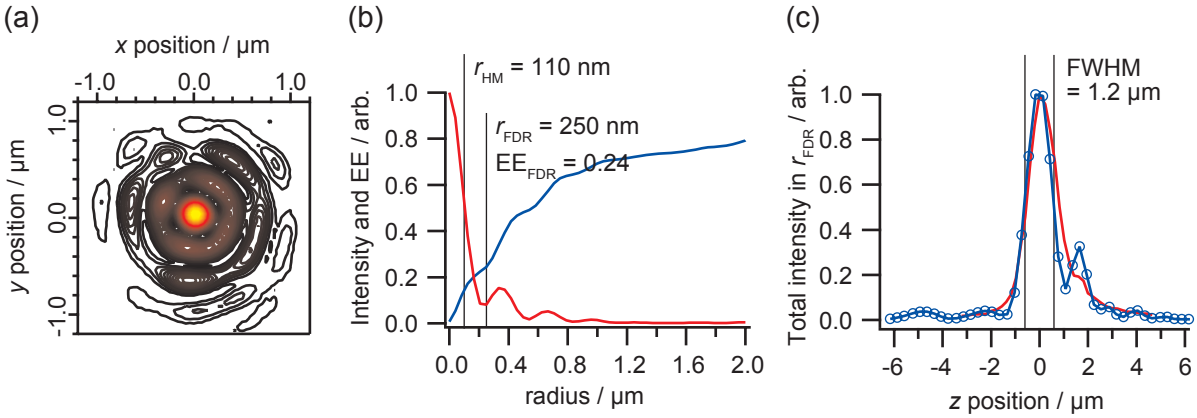

Figure 3.6 Focused spot and spatial resolution of the objective pair of the ARO (No. 2) and MPLAPON50X. (a) Focused spot taken by the CMOS camera (λ = 473 nm). x and y positions are the scale at the focal plane of the ARO. (b) One-dimensional spot. (c) Resolution along the optical axis (z). The integrated intensity in r_{FDR} = 250 nm was plotted versus the distance between the two objectives.

3.1.3 Evaluation of the excitation density of the aspherical reflective objective (ARO)

The conversion factor between the laser intensity [W] and excitation density [W cm^{-2}] at the objective focus is evaluated for the ARO. Figure 3.7a shows the entrance pupil of the

ARO. The pupil is a doughnut shape whose minimum and maximum radii are 1.01 mm and 2.25 mm respectively. Only the rays passing through the pupil are focused by the ARO. Figure 3.7b is the beam profile of the excitation light. The $1/e^2$ diameter of the beam is 5.5 mm. The transmittance of the pupil is plotted versus the $1/e^2$ diameter of a Gaussian beam in Fig. 3.7c. Read from the graph, transmittance of the excitation light is $T_{\mathrm{P}}(5.5\ \mathrm{mm}) = 0.50$. $\mathrm{EE}(r_{\mathrm{FDR}}) = 24\%$ is the fraction of the excitation light gathered in the focal spot (see the last subsection). The total intensity of the focal spot I_{F} is

$$\begin{aligned} I_{\mathrm{F}} &= T_{\mathrm{P}} R_{\mathrm{Al}}^2 \mathrm{EE}(r_{\mathrm{FDR}}) I \\ &= 0.10 I, \end{aligned} \tag{3.9}$$

where I is the intensity of the incident light and R_{Al} is the reflectance of the two aluminum mirrors. The value of R_{Al} is calculated as 92.0% at $\lambda = 478$ nm from ref. [46]. An average excitation density at the focal spot W_{F} is expressed as the quotient of I_{F} divided by πr_{HM}^2, where πr_{HM}^2 is the effective area of the focal spot. $r_{\mathrm{HM}} = 110$ nm is the half-maximum radius (see Fig. 3.6b).

$$\begin{aligned} W_{\mathrm{F}} &= I_{\mathrm{F}} / \pi r_{\mathrm{HM}}^2 \\ &= 0.10 I / \pi (110\ \mathrm{nm})^2, \\ W_{\mathrm{F}} / I &= 2.7 \times 10^8\ \mathrm{cm}^{-2}. \end{aligned} \tag{3.10}$$

270 W cm^{-2} of excitation density is achieved when excitation intensity is 1 μW. The photoluminescence of a single Pr^{3+} was saturated at $W_{\mathrm{Sat}} = 219 \pm 43$ W cm^{-2} (detailed in subsection 4.1.5). The order of 10 to 100 W cm^{-2} was the typical excitation condition for the single-ion measurement.

3.2 Confocal reflecting microscope

In microscopy one of the most effective technique to reduce the background emission of a bulk sample is the confocal arrangement. Figure 3.8 schematically shows the confocal arrangement. The spatial mode of an excitation light is formed by a pinhole (Pinhole1) and transformed to a coherent parallel beam by a collimator lens. The excitation light is reflected by a long-wavelength pass filter used as a dichroic beam-splitting mirror (DM) and focused to a sample by an objective. The emission diverging from the objective focus is collimated by the same objective and goes back the excitation optical path. The emission going through the DM was focused on the entrance aperture of the detection pinhole placed in front of the

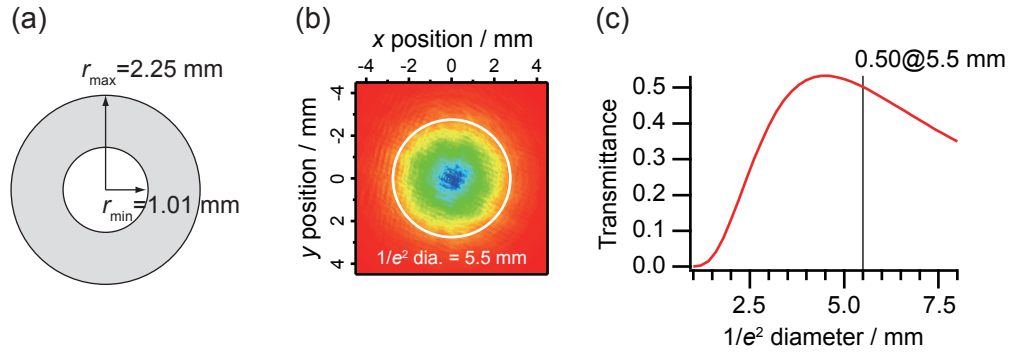

Figure 3.7 Entrance pupil of the ARO and transmittance of the excitation beam. (a) The aspheric convex mirror detracts the circular region with a radius of r_{min} from the entrance pupil. (b) Beam profile of the excitation light taken by a CMOS camera. The $1/e^2$ diameter of 5.5 mm was determined by Gaussian fitting. (c) Transmittance of the entrance pupil for Gaussian beam. The transmittance curve is a convex shape because a thinner beam is blocked by the convex mirror and thicker sticks out from the outer edge of the pupil.

detector (Pinhole2). As shown in Fig. 3.8, emissions from out of the focus are not focused on the detection aperture. Only the emission from the focus is detected sensitively.

Figure 3.9 shows the optical arrangement of the home-build confocal setup dedicated to single Pr^{3+} ion detection in LaF_3 at 1.5 K. The excitation pinhole of this setup is a single-mode optical fiber laid from the excitation lightsource. When the excitation beam passes through a Beam Splitter [BS(95:5)], 5% of the excitation light was reflected to a Photo-Detector (PD). Intensity of the reflected beam was used as the feed-back signal to stabilize the excitation intensity 3.3.4. The polarization angle of the linear polarized excitation light is rotated by the Half-Wavelength Plate (HWP). The ARO in the cryostat focuses the excitation light on the sample surface and collects the luminescence. The collimated luminescence goes through the DM and enters a luminescence imaging system. The luminescence imaging system has two paths switched by the flipper mirror. One is an imaging system using a liquid-nitrogen cooled CCD camera to take a focused image of the luminescence. The other is a combination of a focal lens (f_1 = 150 mm) and a multi-mode fiber working as the detection pinhole of the confocal setup. The excitation light reflected from the entrance surface of the ARO and the sample surface was reflected by the BS and imaged by a reflection imaging system using a CMOS camera. In the following, the luminescence and the reflection imaging systems will be described in detail.

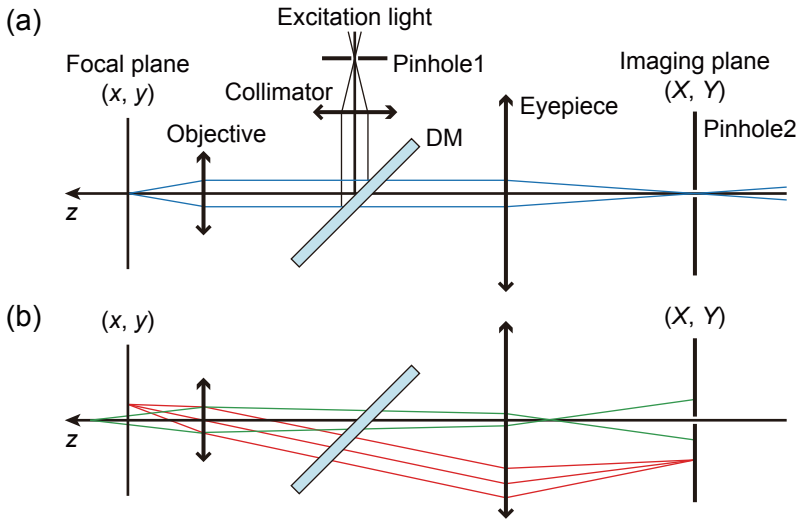

Figure 3.8 Schematic image of the confocal arrangement. (a) Rays of the excitation light (black line) and the emission from the objective focus (blue line) are displayed. (b) Reduction of the emissions from out of the focus. The green line shows the ray coming from a different depth from the focal plane. The red line is the ray coming from a laterally distant position from the focus. Either rays are not focused on the entrance aperture of the detection pinhole and caught by the detector.

3.2.1 Luminescence imaging system

Photo-luminescence detection of a single Pr^{3+} is hampered by luminescence from other Pr^{3+} ions in the crystal. When a large number of emitters distribute homogeneously in a host crystal, background emission comes from the periphery of the objective focus where emitters are weakly excited and even from the whole crystal where emitters are slightly illuminated by an excitation light which is scattered in the crystal. At the focal plane of the luminescence imaging system, emissions from nano-sized emitters such as a single molecule or ion are focused into an expanded image of the focused spot of the objective. This is because the imaging lens has the much longer focal length (i.e. lower NA) than the objective and the quality of luminescence image is solely determined by the focusing performance of the objective. However when emissions from dispersed emitters are simultaneously focused on the imaging plane, such ideal spot never appears because the electromagnetic fields emanating from different emitters do not interfere. Figure 3.10 shows the luminescence spot of the bulk Pr^{3+}:LaF_3 crystal taken by the CCD camera of the luminescence imaging system. The shape of the spot showed the simple structure without concentric dark and bright rings which appeared in the

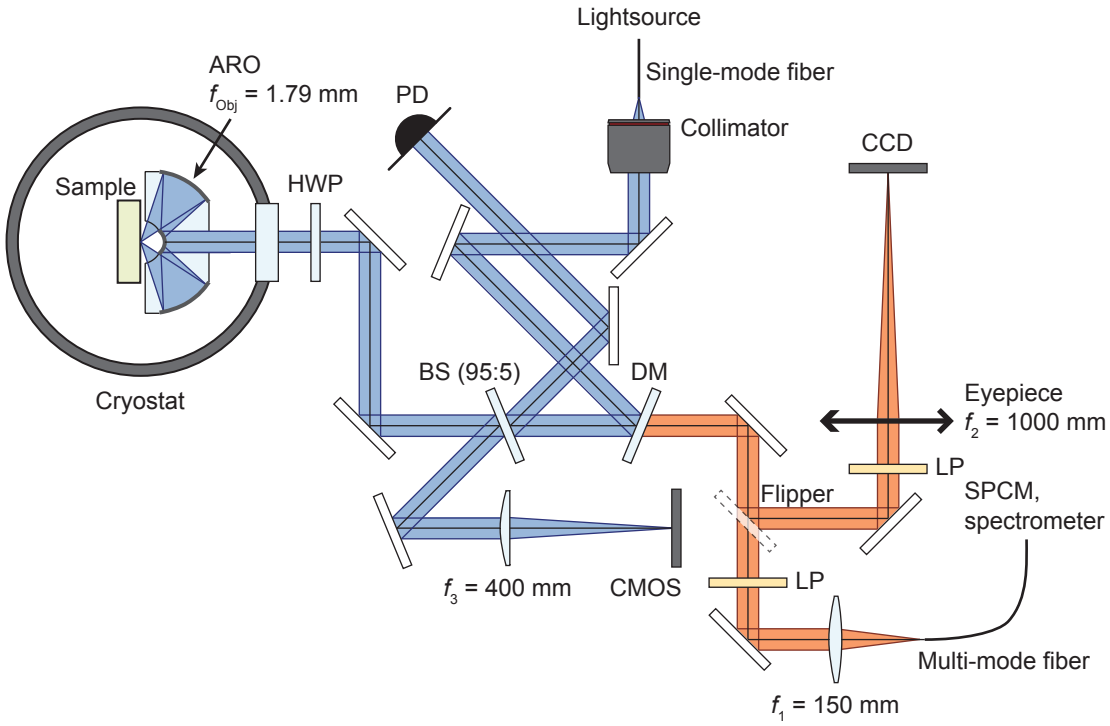

Figure 3.9 Optical arrangement of the home-build confocal setup. Abbreviations are PD: Photo Detector; DM: Dichroic Mirror; BS: Beam Splitter; HWP: Half-Wavelength Plate; ARO: Aspheric Reflecting Objective; CMOS: CMOS camera; LP: Long-wavelength Pass filter; CCD: CCD camera (liquid-nitrogen cooled); SPCM: Single-Photon Counting Module.

focused spot of the ARO.

As already discussed above, the detection pinhole can reduce the background emission from ions out of the focus. Figure 3.11 shows luminescence spots of a single Pr^{3+} ion and the bulk crystal at the entrance surface of the multi-mode fiber. The aperture of the multi-mode fiber (ϕ = 50 μm) is also shown in the figure. The radius of the detection aperture (r_{PH} = 25 μm) was close to the first dark ring of the luminescence spot. The detector only senses the light gathered in the circle with the radius of r_{PH}. For the emitter in the objective focus, the fraction of the emission pass through the multi-mode fiber is EE(r_{PH}) = 24%.

3.2.2 Collection efficiency of the emission from single Pr^{3+}:LaF_3

Detection efficiency of the microscope was evaluated for a single Pr^{3+} ion doped in a LaF_3 crystal. The luminescence emitted by a single Pr^{3+} ion is refracted at the crystal surface and collected by the objective. The proportion of luminescence collected by the ARO is $\Omega/4\pi$ = 0.076 for emitters in a LaF_3 crystal (Tab. 3.2). Taking into account the reflection

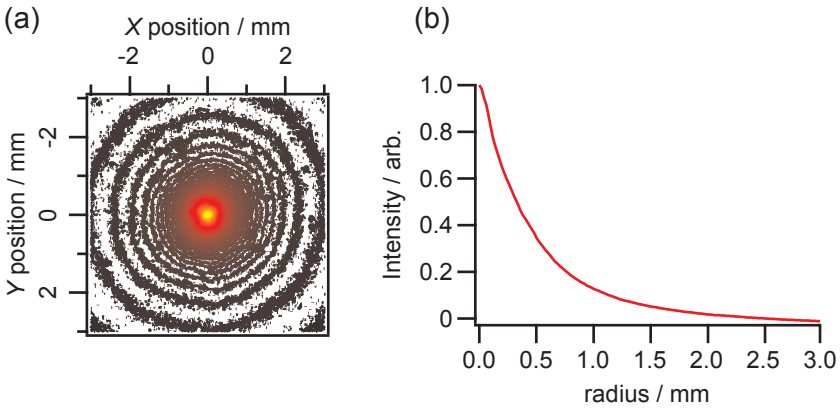

Figure 3.10 Luminescence spot of the bulk Pr^{3+}:LaF_3 at room temperature. (a) Luminescence image taken by liquid-nitrogen cooled CCD camera. The excitation wavelength was 473 nm. X and Y positions are the real scale at the image plane of the CCD. (b) One-dimensional spot.

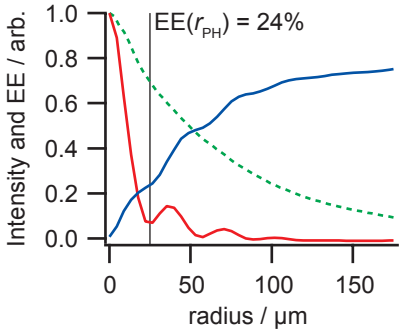

Figure 3.11 Luminescence spots at the entrance surface of the multi-mode fiber. The red line is the virtual luminescence spot of a single Pr^{3+} ion (emission wavelength is 600 nm). This spot was made from the focused spot of the ARO at 473 nm (Fig. 3.6) by scaling the spot-radius by the wavelength (473 nm → 600 nm) and expanding at the magnification ratio of the microscope $f_2/f_{\mathrm{Obj}} = 84\times$. The blue line is EE of the spot. The EE value at the r_{PH} is 24%. The green dashed line is the luminescence spot of the bulk Pr^{3+}:LaF_3 crystal (reproduction of Fig. 3.10b). The horizontal size of the bulk spot is rescaled to the fiber imaging system.

loss at the sample surface R_{surf} and the reflectance of the two aluminum mirrors of the ARO R_{Al}, the collection efficiency of the objective is calculated as below.

$$\begin{aligned} C_{\mathrm{Obj}} &= (1 - R_{\mathrm{surf}}) R_{\mathrm{Al}}^2 \, \Omega/4\pi \\ &= 0.057, \end{aligned} \tag{3.11}$$

where values of R_{Al} at $\lambda = 600$ nm: 0.91 [46] and R_{surf} for the interface of LaF_3 and super-fluid helium: 0.91. R_{surf} was calculated by Fresnel's reflection law with the refractive index

of two matrices ($n_{\mathrm{LaF3}}/n_{\mathrm{He}} = 1.56$) and the incident angles ($\theta_{\max}, \theta_{\min}$ from Tab. 3.2). The transmittance of the all optical components is $T = 0.55$ for the luminescence passing through from windows of the cryostat to the multi-mode fiber of the imaging system. As discussed in the last subsection, only the fraction of $\mathrm{EE}(r_{\mathrm{PH}}) = 24\%$ of the luminescence is gathered in the entrance aperture of the fiber. The transmittance of the entire confocal setup T_{MS} is

$$\begin{aligned} T_{\mathrm{MS}} &= \mathrm{EE}(r_{\mathrm{PH}})\, T \\ &= 0.13. \end{aligned} \tag{3.12}$$

The total detection efficiency of the setup is the product of C_{Obj}, T_{MS} and the quantum efficiency of the SPCM $q = 0.58$.

$$\begin{aligned} C_{\mathrm{MS}} &= q\, C_{\mathrm{Obj}}\, T_{\mathrm{MS}} \\ &= 0.043 \quad (0.43\%). \end{aligned} \tag{3.13}$$

The emission rate of single Pr^{3+} is calculated as $\Gamma = 7.0 \times 10^3$ (2.1), and the luminescence signal intensity is to be

$$\begin{aligned} I_{\mathrm{single}} &= C_{\mathrm{MS}}\, \Gamma \\ &= 29 \approx 30 \text{ cps}. \end{aligned} \tag{3.14}$$

I_{single} can be increased by making the detection aperture r_{PH} i.e. $\mathrm{EE}(r_{\mathrm{PH}})$ larger. Nevertheless, the background emission reaching to the detector also increases quadratically ($\propto r_{\mathrm{PH}}^2$). The signal to noise ratio of a confocal setup improves with a smaller aperture unless the desired signal is much weaker than the dark noise of the detector. The dark count of the two SPCM detectors were 13 cps and 1 cps. The shot noise of the dark count is at most $\sqrt{13}$ cps. With an integration time of 1 s, I_{single} of 30 cps is detectable with the signal to noise ratio of $30/\sqrt{43}$.

3.2.3 Reflection imaging system

The excitation light causes two experimentally important reflections in the cryostat. One is the reflection at the polished incident plane of the ARO and the other is at the surface of the sample crystal (Fig. 3.12a). Two reflected beams go back the path of the incident beam. The BS splits these beams to the reflection imaging system which consists of a plano-convex lens ($f_3 = 400$ mm) and a CMOS camera. Figure 3.12b shows a reflection image taken by the CMOS. The spot in the center is the reflection from the sample surface. This is the expanded

image of the focused spot of the excitation light at the surface. The expansion ratio is the ratio of two focal lengths $f_3/f_{\mathrm{Obj}} = 223\times$. When the objective focus is displaced from the surface, the reflection spot spreads and the brightest spot in the center vanishes (Fig. 3.13). Therefore the reflection image was used to focus the objective to the sample surface. The other reflection spot in the upper-left of Fig. 3.12b is the reflection from the incident plane of the ARO. When the optical axis of the ARO makes an angle of θ with the incident beam, the angle between the reflected beam and the incident beam is 2θ. Because the reflection from the sample always follows back the same path as the incident beam, the angle between two reflected beams is also 2θ. Two reflections are displaced at a distance of $2f_3\theta$ on the CMOS plane. Therefore, the angle θ can be determined from the position of the reflection spots $\boldsymbol{R} = (X,Y)$.

$$\theta = R/2f_3. \tag{3.15}$$

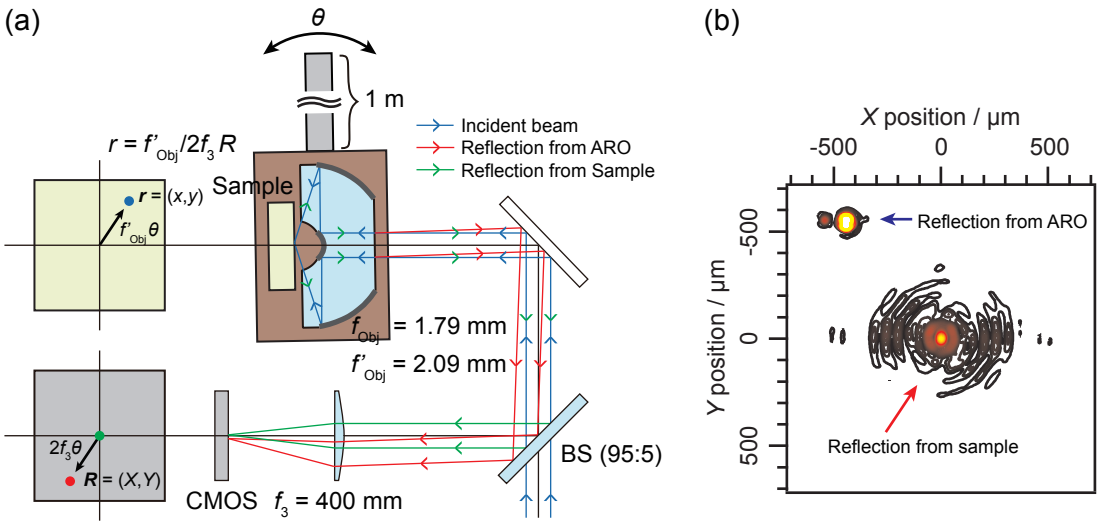

Figure 3.12 Reflection imaging system. (a) Schematic of the setup and incident/reflected beams. Line colors correspond to; light blue: incident excitation light; dark blue: reflection from the sample surface; red: reflection from the entrance plane of the ARO. (b) Reflection image taken by the CMOS camera. X and Y positions are the real scale at the image plane of the CMOS.

The sample and the objective are mounted on a single component holder with a hinge mechanism. The contradictory requirements of fine focus tuning and mechanical stability both on the level of the diffraction-limited resolution were simultaneously fulfilled: The hinge mechanism enables fine adjustment of the distance between sample and objective and the robust single-component construction of the holder guarantees the stability over hours [47].

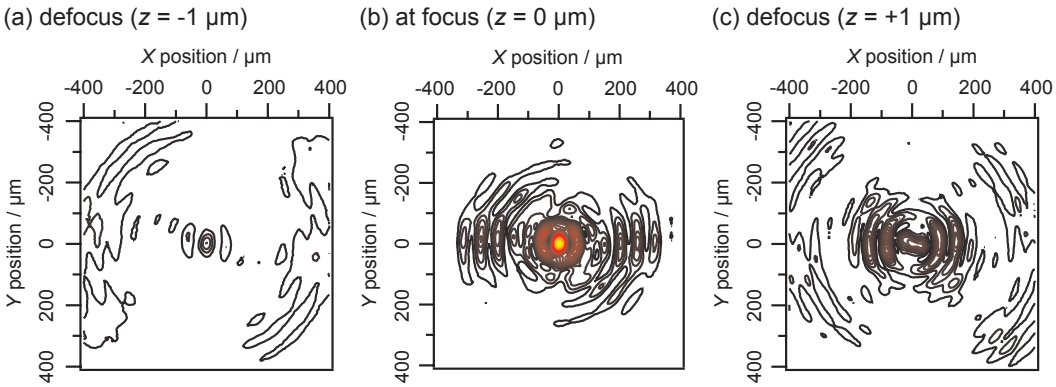

Figure 3.13 Adjustment of the objective focus using reflection images. Reflection images were taken at different sample positions (z). $z = 0$ is defined to the position where the best focused image (b) was taken. The sample is closer to the objective when z is larger. (a) $z = -1$ μm. (b) $z = 0$ μm. (c) $z = +1$ μm.

However, leaning of the insert unit is measurable because the unit is hanged in the cryostat by a stainless rod as long as 1 m. The position of the objective focus $\boldsymbol{r} = (x, y)$ glides $f'_{\mathrm{Obj}}\theta$ on the sample surface, which means

$$\theta = r/f'_{\mathrm{Obj}}, \tag{3.16}$$

where θ is the lean angle of the insert and $f'_{\mathrm{Obj}} = 2.09$ mm is the proportional constant between r and θ. In contrast to the ideal lens (so-called $f\theta$ lens), the aspheric design causes the disagreement between f'_{Obj} and the focal length f_{Obj}. The relation between the position of the objective focus and the position of the reflection spot is derived from eqs. (3.15) and (3.16).

$$\begin{aligned} r/f'_{\mathrm{Obj}} &= R/2f_3 \\ r &= (f'_{\mathrm{Obj}}/2f_3)R. \end{aligned} \tag{3.17}$$

$f'_{\mathrm{Obj}}/2f_3 = 96\times$ is the magnification ratio between $\boldsymbol{r}$ and $\boldsymbol{R}$. Drift of the objective focus due to leaning of the insert unit can be predicted from the reflection image.

Figure 3.14 shows the influence of the thermal strain of the insert on the focal position. Position of the objective focus and the temperature of the cryostat were monitored for 2 hours in a vacuum cooling process after the superfluid translation of liquid helium injected in the cryostat. Figure 3.14a is a trace of focal position on the sample surface measured by the reflection imaging system. Plots of x and y positions are particularly displayed in Fig. 3.14b with the temperature of superfluid helium. As cooling progressed, the focal position drifted

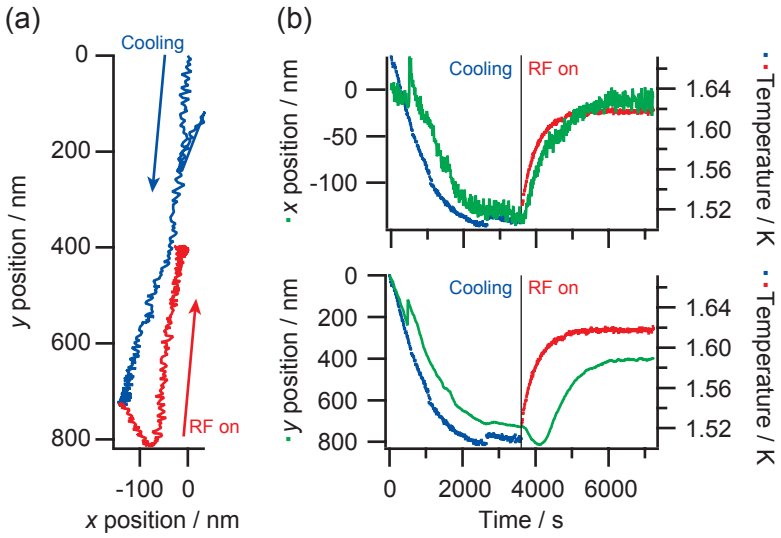

Figure 3.14 Thermal strain of the insert unit monitored for 2 hours in a vacuum cooling process of superfluid helium. (a) Trace of focal position $\boldsymbol{r} = (x, y)$ measured by the reflection imaging system. RF irradiation was applied after 1 hour elapsed from acquisition started. (b) Plots of x and y positions with the temperature.

downward about 0.8 μm. RF irradiation for Pr nuclear spin resonance [11] was applied after 1 hour elapsed from acquisition started. Few watts of RF power was dissipated as heat in the cryostat, and rising of the temperature caused regress of the focal position. Measurement of a single nano-sized emitter can not be carried with the drift of the focal position larger than the spot diameter (200 nm). Single-ion measurements were conducted 1-2 hours after the superfluid transition to wait cooling of the cryostat. It was also revealed that RF irradiation is unsuitable to excite a single Pr nuclear spin because the temperature fluctuation associated with the switching of RF causes the non-negligible drift of the focal position.

3.3 Excitation lightsource

The homogeneous width of Pr^{3+}:LaF_3 narrows down to the lifetime-limited width Γ_h = 10 kHz at 1.5 K. The finesse of the spectral line ν_0/Γ_h exceeds 10^{10}, where ν_0 = 627.33 THz is the absorption frequency of the ${}^3H_4 \rightarrow {}^3P_0$ transition. To excite such a sharp spectral line efficiently, the linewidth of an excitation lightsource, which means the width of laser frequency fluctuation, must be kept low comparable with the spectrum because the laser frequency component which spreads out the spectrum never contributes to the excitation. To maintain the measurement of a single Pr^{3+} for a few hours, drift of the laser frequency also needs to be controlled smaller than the laser linewidth itself. Therefore, the narrow-linewidth laser system was built for the single-ion spectroscopy of Pr^{3+}:LaF_3. The laser linewidth was kept down to 0.4 MHz in FWHM and the long-time stability of the laser frequency was ±0.018 MHz/day.

Figure 3.15 shows the home-build lightsource. A continuous-wave (CW) diode laser (DL pro, Toptica) is a fundamental lightsource of the system. A MgO-doped Periodically Poled $LiNbO_3$ (PPLN) waveguide converts Near Infrared Red (NIR) output of the diode laser (956 nm) to the visible excitation light (478 nm) by the second harmonic generation (SHG). An optical cavity is a frequency reference to stabilize the output frequency (wavelength) of the diode laser. To conduct the excitation spectroscopy of a single Pr^{3+}, frequency scanning of the excitation light must be carried while the fundamental laser is locked to the frequency reference. Two Acousto-Optic Modulators (AOMs) diffracts the excitation laser exiting the PPLN waveguide to shift the excitation frequency. One of the two AOMs is also used to stabilize the excitation intensity to improve the clarity of the excitation spectrum.

3.3.1 Laser system

DL pro, the fundamental lightsource, is a single-mode CW diode laser. The whole length of the laser system is only 24 cm and principal components such as a laser diode (LD) and an external resonator (grating) are assembled in a laser head smaller than 10 cm (Fig. 3.16). The compact chassis benefits on a stability of output frequency. The nominal value of the laser linewidth is 100 kHz/5 μs. This narrow linewidth can be utilized to resolve the hyperfine structure of Pr^{3+} (about 10 MHz) and excite a small part of Pr^{3+} ions in the objective focus by the frequency selection.

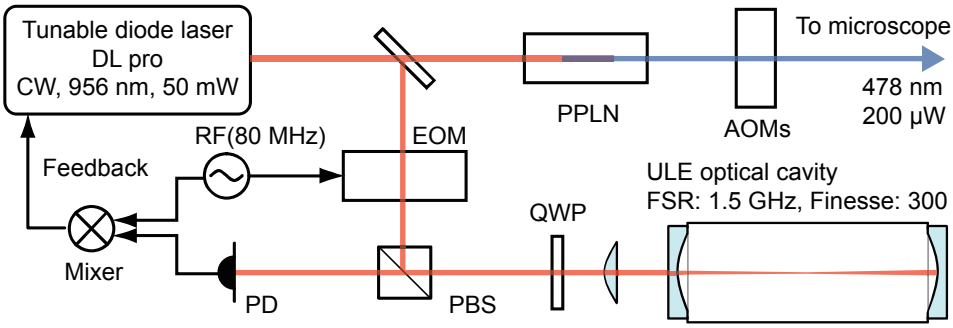

Figure 3.15 Schematic of the home-build excitation lightsource. Abbreviations are CW: Continuous Wave; PPLN: MgO-doped Periodically Poled $LiNbO_3$ waveguide; AOMs: Acousto-Optic Modulators; EO Modulator: Electro-Optic Modulator; RF: Radio Frequency; PBS: Polarized Beam Splitter; QWP: Quarter wave plate; FSR: Free Spectral Range; PD: Photo Detector.

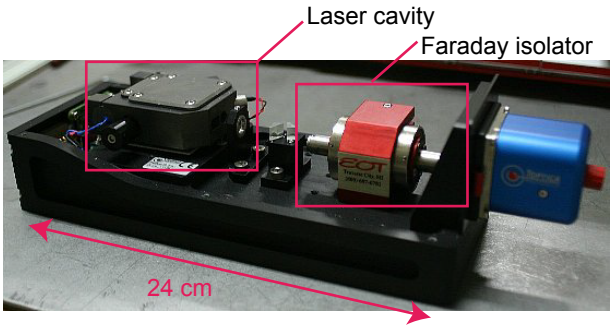

Figure 3.16 Inside of the tunable diode laser DL pro. Faraday isolator protects the laser cavity from the backward-moving light reflected from the latter part of the setup such as the PPLN waveguide.

The waveguide-type PPLN crystal (HC Photonics) is employed to the wavelength conversion. The fundamental light goes through a single-mode waveguide fabricated on the PPLN crystal. Because the SHG efficiency is proportional to the input energy density, the fundamental laser is converted to the SHG light more efficiently in the tight waveguide (10 μm of mode-diameter) than bulk PPLN crystals. Figure 3.17 represents the arrangement of the PPLN and peripheral components. The NIR output of the diode laser is coupled to the waveguide by a lens pair and an objective. The converted SHG light and the unconverted fundamental are collimated and spitted to each other by a short-wavelength-pass filter. The SHG light goes to the latter stage. The wavelength of the fundamental is measured by a wavelength meter (WA-20VIS, Burleigh). The SHG wavelength is to be a half of the fundamental wavelength. Figure 3.18 shows a photograph of the waveguide PPLN. The fundamental comes from the left side of the photo and the SHG light flies rightward from the PPLN. 2-3 mW

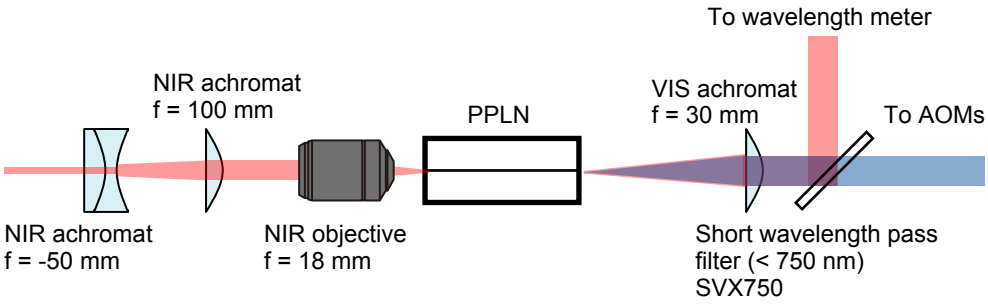

Figure 3.17 Optical arrangement of the PPLN wavelength converter.

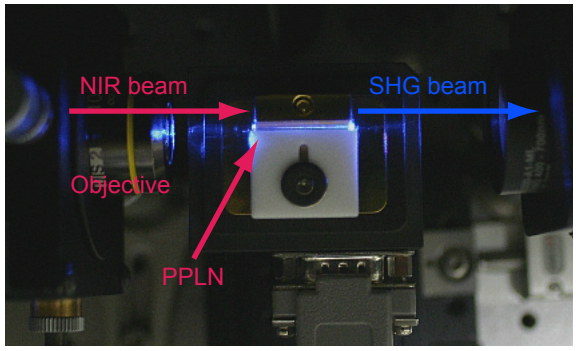

Figure 3.18 Wavelength conversion using the PPLN crystal.

of the SHG light was yielded from 50 mW of the fundamental NIR light. The hole-burning measurement of Pr^{3+}:LaF_3 revealed that the frequency-stabilized SHG light had a FWHM linewidth of 0.4 MHz.

3.3.2 Laser frequency stabilization using ULE cavity

The output frequency of the laser is exposed to environmental perturbations such as the temperature change and the mechanical vibration. Under the temperature constant up to 100 MHz/K, it is difficult for the free-running laser to ensure the frequency stability exceeding its linewidth (< 100 kHz). The laser frequency needs to be locked to a certain robust frequency reference.

The optical cavity is the frequency reference of the home-build lightsoure. The cavity consists of a cylinder made from Ultra Low Expansion (ULE) glass (Corning) and two high-reflectance (but partially transmissive) mirrors attached on both ends of the cylinder. These

mirrors work as a Fabry-Perot Cavity. The transmittance of the cavity is

$$T(\delta) = \frac{(1-R)^2}{(1-R)^2 + 4R\sin^2(\delta/2)}, \delta = \frac{4\pi L}{\lambda} = \frac{4\pi L\nu}{c}, \tag{3.18}$$

where R is the intensity reflectance of the mirrors, L is the length of the cavity, c is the speed of light and λ (ν) is the laser wavelength (frequency). The maximal transmittance is realized when $\sin(\delta/2) = 0$, that is

$$\delta/2 = n\pi \tag{3.19}$$

$$\nu_n = \frac{nc}{2L} = n \cdot \mathrm{FSR}, \tag{3.20}$$

where n is an integer. The transmittance of the cavity has peaks formed at regular intervals called Free Spectral Range (FSR), which is determined by the cavity length L. The width of these transmission peaks is

$$\Delta\nu = \frac{2}{\pi}\sin^{-1}\left(\frac{1-R}{2\sqrt{R}}\right). \tag{3.21}$$

The ULE cavity used in the lightsource has the cavity length $L = 100$ mm and the mirror reflectance $R = 98.96\%$. Substituting these values to (3.20) and (3.21)

$$\mathrm{FSR} = 1.5\ \mathrm{GHz}, \tag{3.22}$$

$$\Delta\nu = 5\ \mathrm{GHz}. \tag{3.23}$$

The finesse of the transmission peaks is $\Delta\nu/\mathrm{FSR} = 300$.

Figure 3.19 shows the transmission spectrum of the ULE cavity, which was measured by 1.5 GHz scanning of the output frequency of DL pro. Inset images are profiles of the transmitted beam taken at each peak frequency. The strongest peak is correspond to the lowest Gaussian mode of the cavity, which appeared at an interval of the FSR (1.5 GHz). There are another four peaks appearing at an interval of 0.3 GHz, which correspond to the higher-order spatial modes. These peaks appears because the spatial mode of the laser did not accord with the lowest Gaussian-mode perfectly.

The fundamental diode-laser frequency was locked to the ULE cavity using the Pound-Drever-Hall method [48]. Figure 3.20 shows the optical arrangement of the ULE cavity and peripheral components. The beam splitter mounted on the isolator splits about 100 μW of the laser light. The phase of the laser light is modulated by a EOM. The Modulation frequency is 80 MHz. The beam passing through a PBS and a QWP is coupled to the cavity. The transmitted light is detected by PD1. The reflection from the cavity passes through the QWP

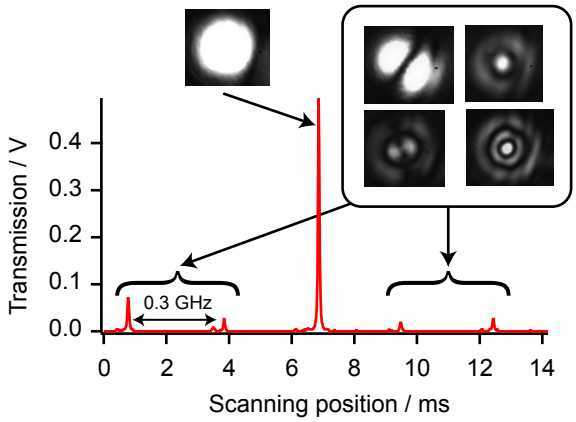

Figure 3.19 Transmittance of the ULE cavity. The vertical axis is the transmission intensity taken by the photo-detector. The horizontal axis is the frequency-scanning position of the tunable laser. The scanning speed is approximately 1 GHz/ms.

again, and its linear polarization angle is made orthogonal to that of the incident light. The reflection is reflected by the PBS and detected by PD2. The feedback signal input to the laser is made by mixing the reflection signal and the modulation RF signal. Figure 3.21 shows the transmission spectrum of the lowest Gaussian mode (blue curve) and the feedback signal (red curve) as a function of the laser scanning position of the phase-modulated laser. The cavity transmittance appears in a three-pronged shape. This is because the phase modulation brings the modulated light the frequency sidebands. The frequency detuning between the fundamental and the sideband corresponds to the phase modulation frequency (80 MHz). The sign of the feedback signal flips at the peak frequency of the fundamental, therefore, the feedback signal can read the laser frequency is whether high or low relative to the cavity reference frequency while the simple transmittance brings only the degree of detuning from the reference.

When the frequency stabilization is actually conducted, the thermal expansion of the ULE cavity becomes a problem to overcome. Because the resonance frequency of the cavity (ν_n) is determined by the cavity length, the temperature drift cause the drift of the feedback reference. The temperature constant of ν_n is calculated as below.

$$\frac{\Delta\nu_n}{\Delta T} = \frac{\Delta\nu_n}{\Delta L} \cdot \frac{\Delta L}{L\Delta T} \cdot L, \tag{3.24}$$

where $\frac{\Delta\nu_n}{\Delta L}$ is the rate of change of the reference frequency with respect to the cavity length L

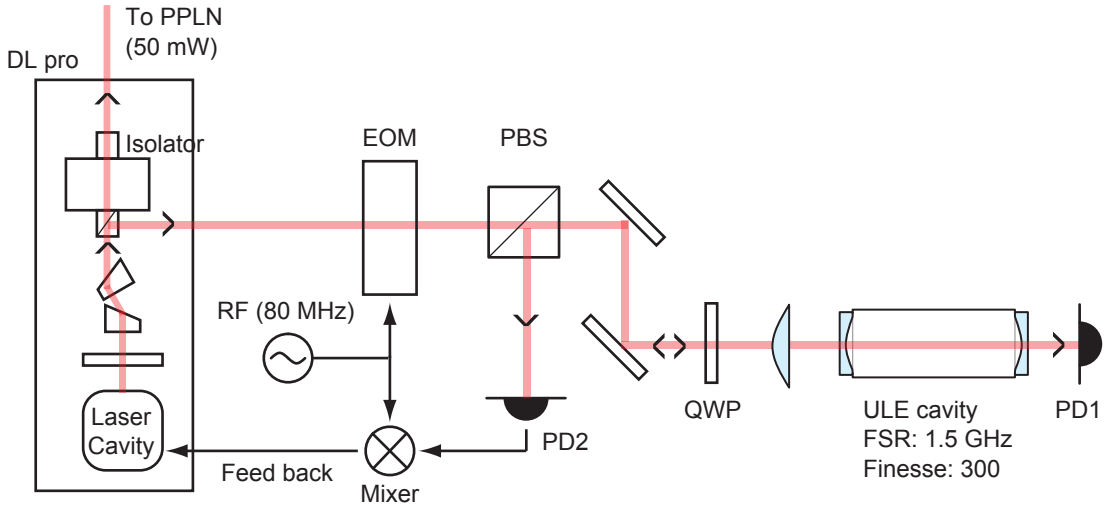

Figure 3.20 Optical arrangement of the laser-frequency feedback system.

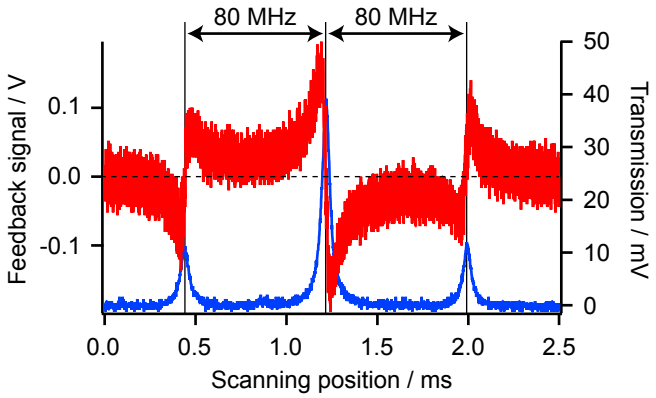

Figure 3.21 Cavity transmittance and feedback signal of the PDH method. The blue curve is the transmission intensity of the phase-modulated laser taken by PD1 (right axis). The red curve is the feedback signal made by mixing the reflection signal and the modulation RF signal (left axis). The horizontal axis is the frequency-scanning position of the tunable laser. The scanning speed is approximately 100 MHz/ms.

and $\frac{\Delta L}{L\Delta T}$ is the linear expansion coefficient of the ULE grass. $\frac{\Delta \nu_n}{\Delta L}$ is derived from (3.20).

$$\nu_n = \frac{nc}{2L} \tag{3.20}$$

$$\frac{\Delta \nu_n}{\Delta L} = -\frac{nc}{2L^2} = -\frac{\nu_n}{L} \tag{3.25}$$

Substituting (3.25) to (3.24),

$$\begin{aligned}\frac{\Delta\nu_n}{\Delta T} &= -\frac{\nu_n}{L}\cdot\frac{\Delta L}{L\Delta T}\cdot L \\ &= -\nu_n\cdot\frac{\Delta L}{L\Delta T}\end{aligned} \tag{3.26}$$

The laser frequency is about $\nu_n = 300$ THz (corresponds to $\lambda_n = 1$ μm) and the linear expansion coefficient of the ULE grass is smaller than $\frac{\Delta L}{L\Delta T} = 3\times10^{-8}$ K^{-1}. Finally,

$$\begin{aligned}\frac{\Delta\nu_n}{\Delta T} &= -300\text{ THz}\cdot 3\times10^{-8}\text{ K}^{-1} \\ &= -9\text{ MHz/K}\end{aligned} \tag{3.27}$$

The ULE cavity is installed in a temperature controlled vacuum chamber (Fig. 3.22a, b). The temperature of the chamber is monitored by a thermistor and controlled by a heater. As a result of the feedback control using a home-build temperature controller, the temperature drift is held down below ±2 mK/day (Fig. 3.22c). It corresponds to the frequency drift of ±0.018 MHz/day, which is a sufficient stability compared with 100 kHz of the laser linewidth in nominal value.

3.3.3 Laser-frequency scanning using AOMs

The excitation frequency scanning is carried by using Acousto-Optic Modulators (AOMs). An Radio Frequency (RF) electric field input to an AO crystal generates a compression wave in the crystal, which functions as a grating. The laser beam is diffracted by this grating, and the laser frequency is shifted as much as the frequency of the modulation RF signal. The frequency scanning of the diffracted light can be conducted by scanning the RF frequency.

Figure 3.23 represents the setup of the laser-frequency shifter using two AOMs. The *p*-polarized SHG light from the PPLN passes through the PBS and diffracted by two AOMs. AOM1 (1205-C2, Isomet) brings the laser frequency an up-shift $+f_1$ and AOM2 (A-140-488, Hoya-Schott) brings a down-shift $-f_2$. The diffracted beam is reflected backward by a lens and a mirror. A QWP changes the polarization of the beam from the *p*-polarization to the *s*-polarization. The reflected beam is diffracted by two AOMs again. This double-pass configuration doubles the frequency shift. The frequency shift given by two AOMs is

$$\Delta f = 2(f_1 - f_2). \tag{3.28}$$

The PBS reflects the twice-diffracted *s*-polarized beam to a single-mode optical fiber which transports the excitation light to the microscope. The double-pass configuration also benefits

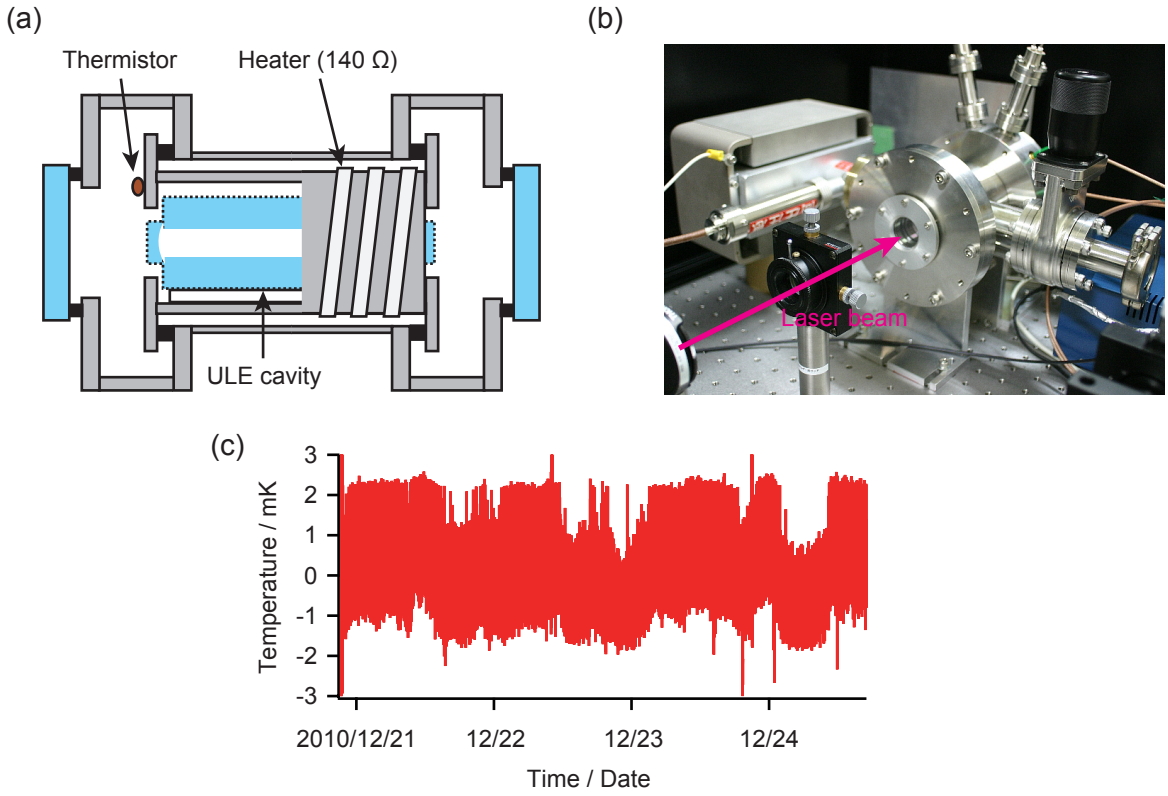

Figure 3.22 Temperature stabilization of the ULE cavity. (a) Schematic of the vacuum chamber and the cavity. (b) Exterior of the chamber. (c) Trace of the chamber temperature over 3 days. The vertical axis is the temperature represented as the difference from the set-point (about 29.9 °C).

the constant coupling to the single-mode fiber. The diffracted-beam direction depends on the input RF frequency. The change of the optical path deteriorates the coupling to the fiber, but the double-pass configuration cancels it. Figure 3.24 shows the laser intensity monitored by the photo-detector build in the microscope as a function of the frequency shift given by two AOMs. When a half maximum width is defined as an effective scanning range, the scanning range of AOM1 is $f_1 = 73 - 93$ MHz and that of AOM2 is $f_2 = 62 - 92$ MHz.

3.3.4 Laser-power stabilization

To detect the weak photo-luminescence of a single Pr^{3+}, in addition to the mechanical stability of the microscope and the frequency stability of the excitation laser, the intensity stability of the excitation laser also needs to be improved. As shown in the red curve in Fig. 3.25a, the output intensity of the excitation laser drifts over 10%. To decrease the instability of the

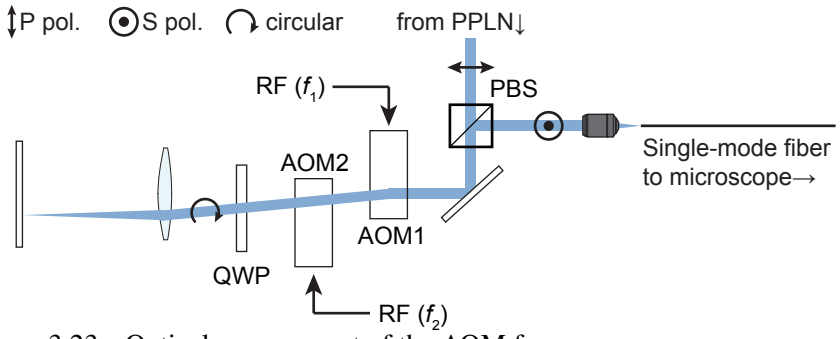

Figure 3.23 Optical arrangement of the AOM frequency scanner.

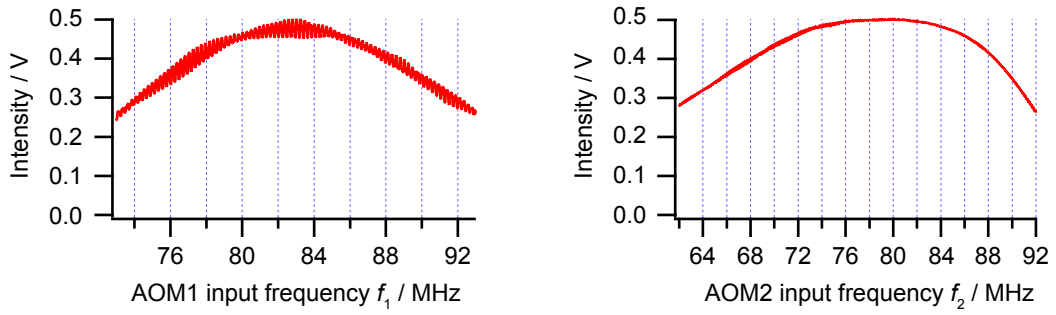

Figure 3.24 Intensity of the excitation light going through the single-mode fiber. The photodetector installed in the microscope (see Fig. 3.9) monitored the intensity while the AOM input frequencies f_1 and f_2 were scanned. (left) As a function of the AOM1 input frequency f_1. f_2 is set to 77 MHz. (right) As a function of the AOM2 input frequency f_2. f_1 is set to 83 MHz.

excitation intensity, the feedback control was applied (the blue curve in Fig. 3.25a). Details of the feedback system using the AOM are described below.

Figure 3.26 shows the laser intensity feedback system. Red dashed circles represent sources of the intensity fluctuation of the lightsource. It is hard to suppress the instability of the coupling efficiency to micrometer-sized waveguides such as the PPLN crystal and the single-mode optical fiber. The photo detector (PD) in the microscope monitors the laser intensity and its output is acquired by a Data ACquisition device (DAC) connected to the PC. The control program (Labview) outputs the feedback signal to the function generator via the analogue output of the DAC. The amplitude modulation (AM) function of the function generator is employed to regulate the amplitude of the RF output to the AOM2. Finally, the laser intensity diffracted by the AOM2 is adjusted to the desired value. The interval of the feedback control is 10 ms. This value is determined by the maximum output sampling rate of the DAC (100 Hz).

Figure 3.25b shows results of the feedback control. The vertical axis represents the stan-

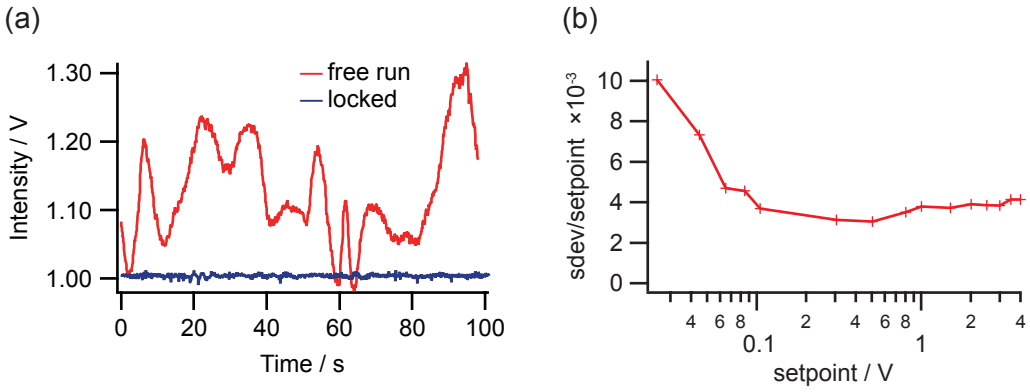

Figure 3.25 Feedback control of the laser intensity. (a) Trace of the laser intensity for 100 s. The red curve is the intensity of the free-running laser. The blue curve shows the intensity under the feedback control. (b) Quality of the feedback control. The vertical axis represents the standard deviation (sdev) of the stabilized laser intensity normalized by the intensity itself (setpoint). 1 V of the PD signal corresponds to 75 W cm^{-2} of the excitation intensity at the objective focus.

dard deviation (sdev) of the stabilized laser intensity normalized by the intensity itself (setpoint). 1 V of the PD signal corresponds to 75 W cm^{-2} of the excitation intensity at the objective focus. In the high intensity region ($>$ 0.1 V), the stability of the laser intensity reached to sdev/setpoint = 0.4%. The quality of the feedback got worse in the low intensity region. This is because the PD signal of the weak laser was buried in the noise from the PD and other electronics.

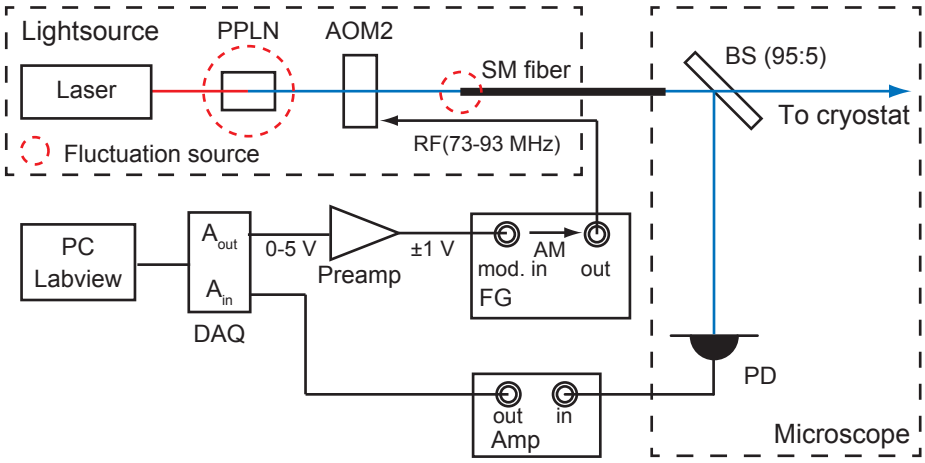

Figure 3.26 Feedback system of the laser intensity using the AOM. Abbreviations are SM fiber: Single-Mode optical fiber; DAQ: Data ACquisition device (USB6009, National Instruments); $A_{in/out}$: Analogue input/output; FG: Function Generator (AFG3252, Tektronix); AM: Amplitude Modulation.

Chapter 4

Results and discussion

The low temperature spectroscopy of single Pr^{3+}:LaF_3, the main subject of the thesis, is described here. Photo-luminescence excitation spectra of individual Pr^{3+} ions were observed at the frequency region distant about +0.01 THz from the center of the inhomogeneously broadened spectrum of the ${}^3H_4 \rightarrow {}^3P_0$ transition. Intensities of the luminescence peaks are $20 - 30$ cps and their widths were approximately 3 MHz. The contents of this chapter were prepared from the journal article of our group [36] (I. Nakamura *et al*., *Scientific Reports* **4**, 7364, 2014).

4.1 Results

4.1.1 Excitation by the three frequency laser

To conduct the photo-luminescence detection of a single Pr^{3+}, the nuclear-spin population transfer caused by the optical excitation (so-called the optical pumping) needs to be settled. Figure 4.1a shows the simplified energy diagram of Pr^{3+}. No matter to which hyperfine sublevel the Pr^{3+} ions are excited, the excited ions relax to all the three ground-state sublevels. Therefore, excitation by a single-frequency laser causes population transfer of the Pr nuclear spin to non-resonant sublevels. The ions stop luminescence until the nuclear spin relaxes back to the resonant hyperfine sublevel, which occurs with a time constant longer than 1 s [49]. The excitation-emission cycle of Pr^{3+} is grossly slowed by the thermal relaxation speed of the nuclear spin state, which is incomparably longer than the radiation lifetime of the excited state (47 μs). The optical pumping effect of ensemble Pr^{3+} ions can be observed by the decrease of photo-luminescence signal. Figure 4.1b shows the photo-luminescence intensity of bulk Pr^{3+}:LaF_3 taken at $\nu_0 = 627.33$ THz by the narrow linewidth lightsouce. When the sample

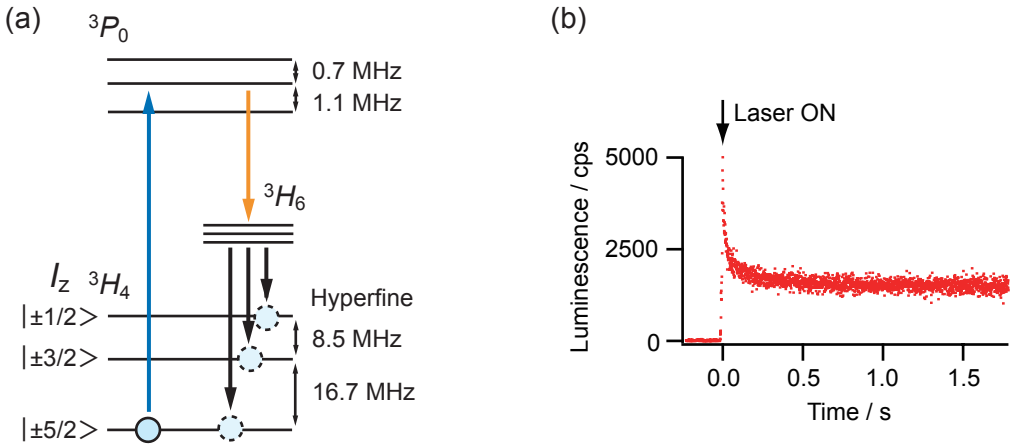

Figure 4.1 Optical pumping of Pr nuclear spin. (a) Simplified energy diagram of Pr^{3+}:LaF_3. Blue circles represent the Pr nuclear spin population. (b) Photo-luminescence intensity of bulk Pr^{3+}:LaF_3. The excitation frequency was ν_0 = 627.33 THz and the excitation intensity is 160 W cm^{-2}.

was illuminated by the excitation light, photo-luminescence intensity immediately dropped to the value where the optical pumping rate and the thermal relaxation rate of the spin came to equilibrium.

In all the experiments described below, the acousto-optic modulator (AOM1) was used as a laser-frequency multiplexer to avoid this quenching. Figure 4.2 shows the method of the laser frequency multiplexing and scanning using two AOMs. The laser-frequency shift given by AOM1 cycles three values, 153.4, 161.9, and 178.6 MHz. The detunings with respect to the lowest frequency component are 0, 8.5, and 25.2 MHz. The excitation with the three frequencies made all the three $^3H_4$ hyperfine sublevels simultaneously resonant with transitions to one hyperfine sublevel of $^3P_0$. The cycling period was set to 30 μs. Because the cycling period is shorter than the lifetime of the $^3P_0$ state (47 μs), for the ions in the excited states, a laser of rapidly cycling frequency can be regarded as light that has three frequency components. Frequency scanning of the three frequency laser was carried by AOM2. AOM2 shifts the laser frequency components downward in the range from -174.0 MHz to -134.0 MHz, and the scanning range ($\Delta\nu$) of 40 MHz is achieved.

4.1.2 Photo-luminescence excitation spectrum of a single Pr^{3+}

Figure 4.3a shows the photo-luminescence spectrum of 0.05% Pr^{3+}:LaF_3 taken at 1.5 K. The $^3H_4 \rightarrow {}^3P_0$ transition appeared at ν_0 = 627.33 THz (λ_0 = 477.89 nm) with a full-width at

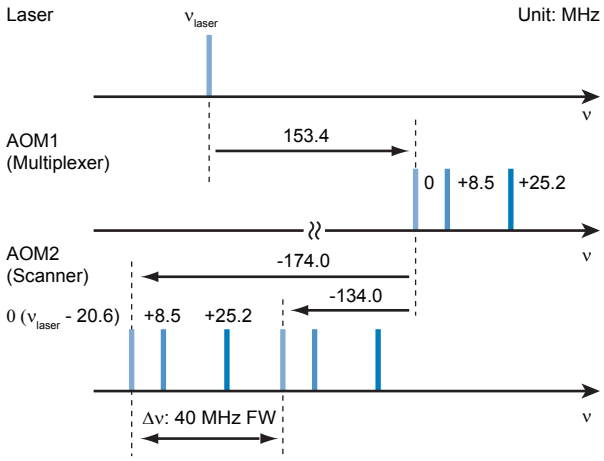

Figure 4.2 Frequency multiplexing and scanning using two AOMs. ν_{laser} is the output frequency of frequency-stabilized laser system. The laser-frequency shift given by AOM1 cycles three values, 153.4, 161.9, and 178.6 MHz with the cycling period of 30 μs (10 μs per one frequency component). AOM2 achieve the 40-MHz scanning by shifting the three laser frequency components downward in the range from -174.0 MHz to -134.0 MHz.

half-maximum (FWHM) linewidth of 12.8 GHz.

Figures 4.3b-g present the photo-luminescence excitation spectra of the Pr^{3+} ions in a confocal volume taken at different frequency positions in the inhomogeneously broadened spectrum of the ensemble of ions shown in Fig. 4.3a. When the excitation spectrum was measured, at frequencies further from ν_0, less resonant ions were in the focus. At a certain frequency, the number of the ions becomes so small that the spectral peaks of individual ions will be observed isolated from each other with the maximum intensity $I_{\mathrm{single}} = 30$ cps (detailed in subsection 3.2.2).

In the measurement shown in Figs. 4.3b-g, a scan of 40 MHz was performed by acquiring photon counts every 0.2 MHz using the single-photon counting module (SPCM). Usually, the photon counts were accumulated for 1 or 2 s, and this scan was repeated 8 or 4 times, respectively, such that the total accumulation time per data point was 8 s. The average of the repeated scans is displayed in the figure. The focus of the setup was adjusted to the surface of the LaF_3 crystal using surface reflection. The total excitation intensity of the three frequency components was approximately 80 W cm^{-2}.

At +0.04 THz from ν_0 (Fig. 4.3b), the average of the signal is approximately 330 cps, and within a 40 MHz scan, the signal varies in intensity between 300 and 360 cps. At +0.09 THz from ν_0 (Figs. 4.3c and d), the average and variation of the signal decrease to approximately 90 cps and between 70 and 105 cps, respectively. Figures 4.3c and d were taken at different

spatial positions on the crystal surface. At some spatial positions, structures narrower than 5 MHz can be observed. At +0.10 THz from ν_0 (Figs. 4.3e and f), the signal further decreases to an average between 60 and 90 cps. Figures 4.3e and f were taken at different spatial positions at the crystal surface. On top of the frequency-independent flat signal at the average intensity, a couple of peaks with heights of approximately 20 cps and FWHMs of approximately 3 MHz appear. For the flat part of Fig. 4.3f between -5 and +15 MHz, the average signal intensity is 90.7 cps, and the standard deviation (sdev) is 4.3 cps. The deviation from the average can be explained as Poisson noise of the flat signal and that of the dark count of the detector of 12.3 cps, which was subtracted before, as observed in the figure. Note that the photon-count accumulation time was 8 s. Apart from the contribution from the flat signal and the dark count, the spectrum consists of only a couple of isolated peaks of 15 - 25 cps. At +0.14 THz from ν_0 (Fig. 4.3g), the signal decreases further to approximately 40 cps and is almost completely flat without peaks with the size observed in Figs. 4.3e and f. Two peaks appeared in Fig. 4.3e at +2.8 and +16.4 MHz are probably signals of individual Pr^{3+} ions. There are some other experimental results which support the interpretation of the peaks as signal from single ions.

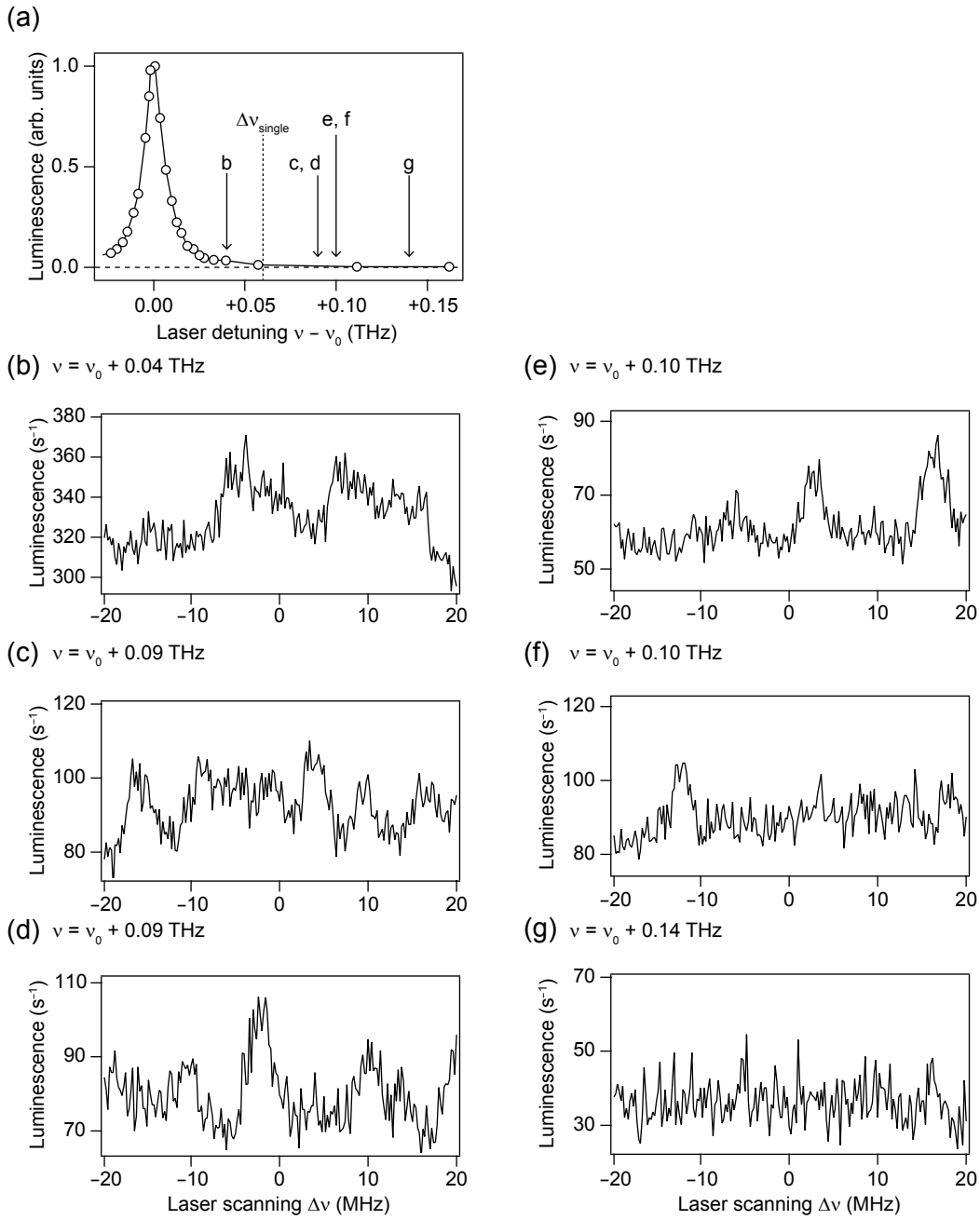

Figure 4.3 Photo-luminescence excitation spectrum of 0.05% Pr^{3+}:LaF_3 at 1.5 K. (a) The inhomogeneously broadened spectrum of the $^3H_4 \rightarrow {}^3P_0$ transition. The horizontal axis represents the laser frequency as detuning from $\nu_0 = 627.33$ THz, the center of the inhomogeneous broadening. The width of the spectrum is 12.8 GHz in FWHM. (b-g) High resolution spectra taken at various frequency positions in the inhomogeneously broadened profile of the ensemble displayed in (a). The horizontal axis represents the laser frequency scanned by AOMs, and ν_c is the center of the scanning range. The vertical axis represents the photon number detected by the SPCM. The dark count of the SPCM was subtracted before the figure was created. The total intensity of the three frequency components was 75-79 W cm^{-2}.

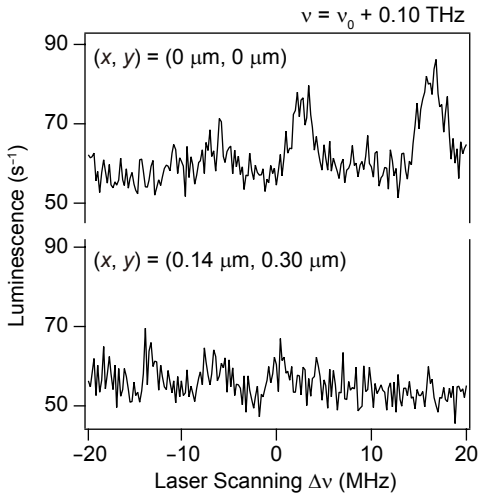

Figure 4.4 Spatial dependence of the excitation spectrum. The upper curve shows the same spectrum as that presented in Fig. 4.3. The lower curve is the spectrum taken at a different location on the crystal surface from that that used for the upper curve but using the same frequency range. The objective focus was displaced 0.14 μm horizontally and 0.30 μm vertically on the surface of the sample.

4.1.3 Spatial dependence of the excitation spectrum

Figure 4.4 shows the spatial dependence of the excitation spectrum. The upper curve presents the spectrum of Fig. 4.3e, which contains a couple of peaks on a flat signal. The lower curve presents the spectrum taken at a different lateral position in the focal plane. The focus of the objective was displaced 0.14 μm horizontally and 0.30 μm vertically from the position at which the upper curve was measured. The two peaks in the upper curve at +2.8 and +16.4 MHz disappear in the lower curve. The lateral size of the focus of the objective was evaluated at 532 nm to be 0.21 μm (subsection 3.1.2). Because the two peaks disappear when the focus moves more than its size, luminescence yielding the two peaks emanates from the focus of the objective. By contrast, because the flat signal does not change when the focus moves, the flat signal originates from the out-of-focus volume of the bulk sample.

4.1.4 Quenching of excitation spectrum due to the optical pumping

Figure 4.5 shows the effect of excitation by three frequency components. The two spectra in the figure were taken at the same spatial position in the crystal as the spectrum of Fig. 4.3e. The three frequency components were 0, 8.5, and 25.2 MHz when recording the black spec-

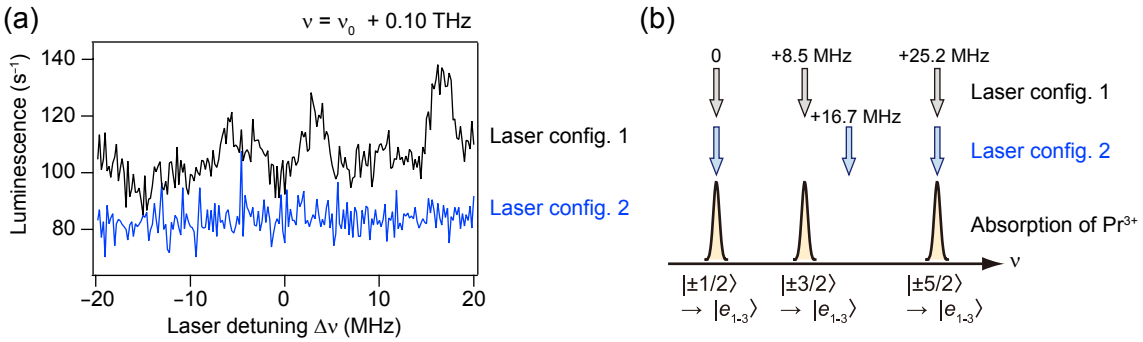

Figure 4.5 Quenching of a photo-luminescence excitation spectrum due to the optical pumping of Pr nuclear spin. (a) Photo-luminescence excitation spectra of the same frequency range as the inset of Fig. 4.3a with a total intensity of 157 W cm^{-2}. The laser configuration of the three frequencies was (0, +8.5, +25.2 MHz, config. 1) for the black curve and (0, +16.8, +25.2 MHz, config. 2) for the blue curve. (b) Schematic of the two frequency configurations of the excitation light (black and blue arrows) and the absorption spectrum of a single Pr^{3+} ion from the three hyperfine sublevels of the ground $^3H_4$ state.

trum and 0, 16.7, and 25.2 MHz when recording the blue spectrum. The two peaks at +2.8 and +16.4 MHz are present only in the black spectrum, not in the blue spectrum. In recording the black spectrum, all three ground-state hyperfine sublevels are in resonance with the excitation light, whereas in recording the blue spectrum, only two of the three sublevels are in resonance, such that the nuclear spin population is transferred to the non-resonant sublevel by the optical pumping, and the resonant sublevels become empty. In the blue spectrum, the flat signal does not completely vanish because many of ions residing in the out-of-focus volume are not subjected to the optical pumping effect due to weak

4.1.5 Saturation behavior and polarization dependence of excitation spectrum

Figure 4.6 shows the saturation and the polarization measurement of a photo-luminescence excitation spectrum. Figure 4.6a is the spectrum taken at +0.08 THz from ν_0. The excitation power dependence was measured for the peak at -3.8 MHz. The luminescence intensity was determined by Gaussian fitting of the excitation spectrum at several different excitation intensities and plotted in Fig. 4.6b. The solid curve is the saturation curve calculated as the steady-state population of the excited state on the assumption that all three ground-state sublevels are in resonance with the excitation light to one of the excited-state sublevels. The

power dependence is expressed as $I(W) = I_{\max} W/(W + W_{\text{sat}}/2)$, where W is the total excitation intensity. The two parameters, the maximum luminescence intensity $I_{\max}$ and the saturation excitation intensity W_{sat}, were determined by fitting to be 45 ± 5 cps and 219 ± 43 W cm^{-2}, respectively. The maximum intensity of 45 cps is consistent with the estimation of I_{single} = 30 cps from the parameters of the bulk measurements. Figure 4.6c shows polarization dependence of the peak at -3.8 MHz in Fig. 4.6a. The luminescence intensity of the peak at -3.8 MHz exhibited a sinusoidal dependence of $\sin 2\theta$, where θ is the polarization angle of the linearly polarized excitation light, while that at -9.0 MHz did not exhibit particular variance. In the present experiment, the laser light propagates parallel to the crystalline c-axis, which has 3-fold symmetry. The Pr^{3+} site symmetry is C_2, and the $^3H_4 \rightarrow {}^3P_0$ transition dipole is along the C_2 axis [28]. Because there are three different C_2 axes in the plane perpendicular to the c-axis, numerous Pr^{3+} ions occupy three different oriented C_2 cites randomly, and in this case, the polarization dependences of the Pr^{3+} ions cancel each other as observed in the measurement of the ensemble of Pr^{3+} ions at the center frequency ν_0 (Fig. 4.6d). Only a single ion and very few ions that are aligned parallel by accident exhibit the deepest modulation to the minimum value of zero.

4.2 Discussion

4.2.1 Summary of the photo-luminescence excitation measurements

The experimental results examined so far support that the 3 MHz-wide peaks of 20 cps, like those recorded in Fig. 4.3e, originate from single Pr^{3+} ions. These peaks were spectrally resolved from the signal of other Pr^{3+} ions contained in the focal volume of the NA = 0.99 objective at the wing of the inhomogeneously broadened spectrum (Figs. 4.3b-g). Emitters yielding these isolated peaks were confirmed to be spatially localized within the focus by moving the focus more than its size (Fig. 4.4). Depending upon the position of the focus, from zero to a few peaks are found in the same frequency region. The peaks appeared only when the excitation laser is in resonance with the transitions of all the three hyperfine sublevels of the ground state (Fig. 4.5). This result confirms that the peaks are the luminescence signals of Pr^{3+} ions and optical control of Pr nuclear spin through optical pumping was demonstrated. The maximum luminescence intensity $I_{\max}$ derived from the power-dependence measurement (Fig. 4.6b) is consistent with the estimation based on the known parameters of the bulk. The polarization dependence (Figs. 4.6c and d) is the same as that expected for a single emitter.

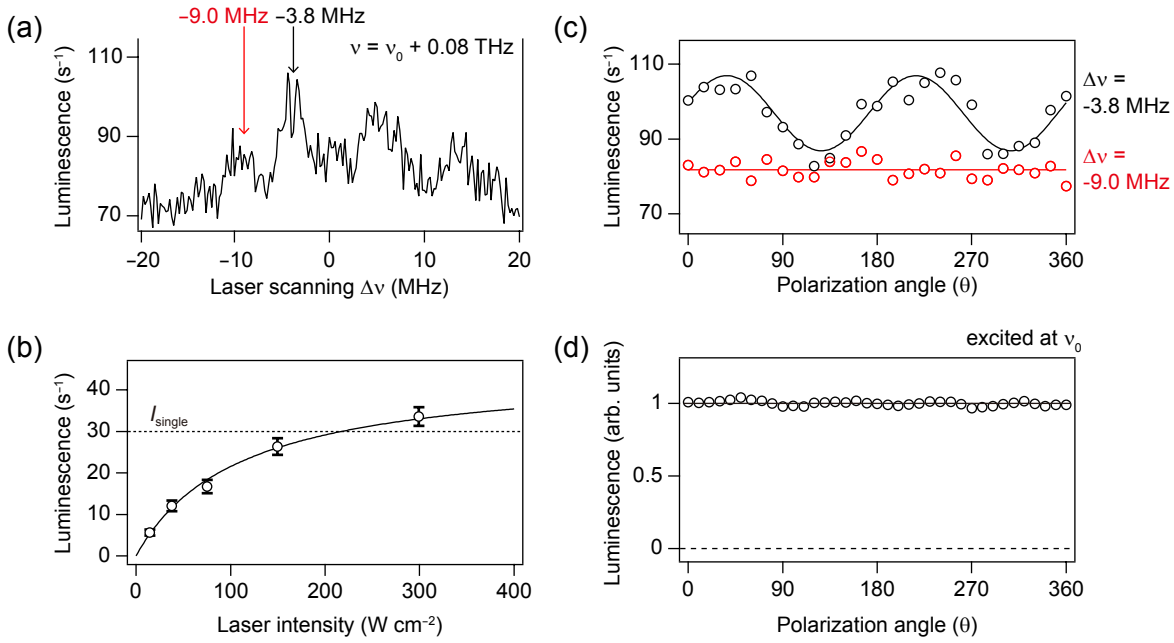

Figure 4.6 Saturation behavior and polarization dependence of an excitation spectrum. (a) Photo-luminescence excitation spectrum of a single Pr^{3+} ion at $\nu = \nu_0 + 0.08$ THz (627.41 THz). The total excitation intensity of the three frequency components was 75 W cm^{-2}. (b) Plot of the luminescence intensity of the peak at -3.8 MHz versus the total excitation intensity (see text for details). The dashed line indicates the signal intensity estimated for single-ion luminescence I_{single}. (c) Plot of the intensity at the peak (excited at -3.8 MHz) and at the wing (excited at -9.0 MHz) versus the polarization angle of the excitation light. The total excitation intensity was 75 W cm^{-2}. The two solid lines indicate sinusoidal fitting of the intensity at the peak and the average luminescence intensity at the wing. (d) Plot of the luminescence intensity of ensemble ions versus polarization angle of the excitation light. The excitation laser was set to ν_0.

4.2.2 Spectral width of single Pr^{3+}

The photo-luminescence excitation spectrum of single Pr^{3+} measured in the present study does not exhibit excited-state hyperfine splitting of 0.7 and 1.1 MHz (Fig. 2.3). The laser carrying three frequency components causes all the three ground-state hyperfine sublevels to be in resonance with the transition to one of the excited-state sublevels. Therefore, the excitation spectrum does not show hyperfine splitting of the ground state but should reflect that of the excited state.

In the hole-burning experiment using the same setup as the single Pr^{3+} experiment, the hole width of 0.4 MHz at low power limit was broadened to 0.8 MHz at the excitation intensity of

40 W cm^{-2}. The photo-luminescence excitation spectra in Figs. 4.3-4.5 were measured with at least 75 W cm^{-2} of excitation intensity. The excitation spectra taken at this power level are considered to be subjected to power broadening to some extent. Other possible mechanisms that cause broadening of the excitation spectrum are spectral diffusion occurring at the interface of the sample crystal and superfluid helium, magnetic interaction with surrounding nuclei, and permanent electric dipole interaction with surrounding Pr^{3+} ions. To investigate the interaction with the surroundings that causes broadening of the single Pr^{3+} spectrum, the excitation intensity must be kept low enough to suppress power broadening. The weakest excitation employed in the present study was 15 W cm^{-2}, and the luminescence signal was only 6 cps. The detection efficiency of the present experiment was too poor. To employ a narrower-linewidth lightsource is also an effective method to take the high-resolution excitation spectrum. However, an higher-finesse optical cavity is required to narrowing the laser linewidth because the low-finesse of the optical cavity (FWHM of 5 MHz) is a bottleneck of the present laser-frequency stabilization.

Chapter 5

Conclusion

Aiming at the optical detection and manipulation of a single rare-earth nuclear spin quantum state, the author conducted the low-temperature spectroscopy of Pr^{3+} doped in a bulk LaF_3 crystal and achieved photo-luminescence detection of individual Pr^{3+} ions. The experiment was carried by a homemade cryogenic setup using a newly developed high-NA objective. The confocal reflecting microscope had the detection efficiency up to 0.43%. To resolve the narrow absorption line of a single Pr^{3+}, the linewidth of the lightsource was made narrower than 0.4 MHz. Spectral lines of the ${}^3H_4 \rightarrow {}^3P_0$ transition of individual Pr^{3+} ions were resolved as luminescence peaks with intensities of $20 - 30$ cps and the full-width at half-maximum of approximately 3 MHz at an excitation intensity of 80 W cm^{-2}. The population transfer of a single Pr nuclear spin was demonstrated via the optical pumping process of the ion.

While the optical addressing of single RE ions has been succeeded in the nanocrystal sample and the single electron transistor (SET), there are certain advantages of the experiment using a bulk crystal sample. However the origin of the broadening is not clear, the width observed in the bulk crystal (3 MHz) is narrower than the FWHM of 14 MHz reported for a Pr^{3+}-doped Y_2SiO_5 nanocrystal [27] and the FWHM of 50 neV (= 12 MHz) reported for a Er^{3+}-doped SET [26]. By considering that the authors of ref. [27] attributed the broadening of the nanocrystal sample to spectral diffusion caused by the strain in the milled crystallites, the high crystallinity of the bulk sample might give the narrow linewidth. A narrower linewidth is in general more favorable in application to quantum information processing because the information density per unit frequency can be increased. The scheme of Rare-Earth Quantum Computer [16] requires a narrow linewidth for quantum logical operation which employs the transition frequency modulation driven by the interaction with other ions.

In the future, when individual RE spins are used as nuclear-spin qubits, an external magnetic field will be applied to the sample to induce the Zeeman effect. Because the Zeeman effect is anisotropic, the orientation of the sample must be accurately controlled. Control of orientation is easier for a bulk crystal than for a nanocrystal.

Bibliography

[1] H. J. Kimble, M. Dagenais, and L. Mandel. Photon antibunching in resonance fluorescence. *Physical Review Letters*, Vol. 39, pp. 691–695, 1977.

[2] W. Neuhauser, M. Hohenstatt, P. Toschek, and H. Dehmelt. Optical-sideband cooling of visible atom cloud confined in parabolic well. *Physical Review Letters*, Vol. 41, pp. 233–236, 1978.

[3] F. Diedrich and H. Walther. Nonclassical radiation of a single stored ion. *Physical Review Letters*, Vol. 58, pp. 203–206, 1987.

[4] R. Lange, W. Grill, and W. Martienssen. Observation of single impurity ions in a crystal. *Europhysics Letters*, Vol. 6, pp. 499–503, 1988.

[5] W. E. Moerner and L. Kador. Optical detection and spectroscopy of single molecules in a solid. *Physical Review Letters*, Vol. 62, pp. 2535–2538, 1989.

[6] J. Köhler, J. A. J. M. Disselhorst, M. C. J. M. Donckers, E. J. J. Groenen, J. Schmidt, and W. E. Moerner. Magnetic resonance of a single molecular spin. *Nature*, Vol. 363, pp. 242–244, 1993.

[7] J. Wrachtrup, C. von Borczyskowski, J. Bernard, M. Orritt, and R. Brown. Optical detection of magnetic resonance in a single molecule. *Nature*, Vol. 363, pp. 244–245, 1993.

[8] R. Kolesov, K. Xia, R. Reuter, M. Jamali, R. Stöhr, T. Inal, P. Siyushev, and J. Wrachtrup. Mapping spin coherence of a single rare-earth ion in a crystal onto a single photon polarization state. *Physical Review Letters*, Vol. 111, p. 120502, 2013.

[9] F. Jelezko, T. Gaebel, I. Popa, A. Gruber, and J. Wrachtrup. Observation of coherent oscillations in a single electron spin. *Physical Review Letters*, Vol. 92, p. 076401, 2004.

[10] F. Jelezko, T. Gaebel, I. Popa, M. Domhan, A. Gruber, and J. Wrachtrup. Observation of coherent oscillation of a single nuclear spin and realization of a two-qubit conditional quantum gate. *Physical Review Letters*, Vol. 93, p. 130501, 2004.

[11] L. E. Erickson. The nuclear quadrupole interaction in Pr^{3+}:LaF_3 — An optical-RF

double resonance measurement of the ground electronic state. *Optics Communications*, Vol. 21, pp. 147–149, 1977.

[12] Y. Takahashi, K. Ishikawa, T. Tanaka, Y. Fukuda, H. Hatanaka, and T. Hashi. Observation of crystal twinning of LaF_3 with Raman heterodyne detection of NMR in Pr^{3+}:LaF_3. *Physical Review B*, Vol. 38, pp. 7121–7124, 1988.

[13] M. Matsushita, A. Mutoh, and T. Kato. Coherent Raman spectroscopy of nuclear quadrupole resonance of La around Pr^{3+} in LaF_3. *Physical Review B*, Vol. 58, p. 14372, 1998.

[14] J. Klein, F. Beil, and T. Halfmann. Robust population transfer by stimulated Raman adiabatic passage in a Pr^{3+}:Y_2SiO_5 crystal. *Physical Review Letters*, Vol. 99, p. 113003, 2007.

[15] R. M. Macfarlane. Inhomogeneous broadening of spectral lines in doped insulators. *Journal of Luminescence*, Vol. 45, pp. 5004–5011, 1990.

[16] N. Ohlsson, R. K. Mohan, and S. Kröll. Quantum computer hardware based on rare-earth-ion-doped inorganic crystals. *Optics Communications*, Vol. 201, pp. 71–77, 2002.

[17] K. Ichimura. A simple frequency-domain quantum computer with ions in a crystal coupled to a cavity mode. *Optics Communications*, Vol. 196, pp. 119–125, 2001.

[18] L. Rippe, M. Nilsson, S. Kröll, R. Klieber, and D. Suter. Experimental demonstration of efficient and selective population transfer and qubit distillation in a rare-earth-metal-ion-doped crystal. *Physical Review A*, Vol. 71, p. 062328, 2005.

[19] H. Goto and K. Ichimura. Observation of coherent population transfer in a four-level tripod system with a rare-earth-metal-ion-doped crystal. *Physical Review A*, Vol. 75, p. 033404, 2007.

[20] R. A. Akhmedzhanov, A. A. Bondartsev, L. A. Gushchin, I. V. Zelensky, and A. G. Litvak. Qubits based on spectrally selected groups of Pr^{3+} ions in a LaF_3 crystal. *JETP Letters*, Vol. 94, pp. 863–867, 2012.

[21] R. Rodrigues-Herzog, F. Trotta, H. Bill, J.-M. Segura, B. Hecht, and H.-J. Güntherodt. Optical microscopy of single ions and morphological inhomogeneities in Sm-doped CaF_2 thin films. *Physical Review B*, Vol. 62, pp. 11163–11169, 2000.

[22] A. P. Bartko, L. A. Peyser, R. M. Dickson, A. Mehta, T. Thundat, R. Bhargava, and M. D. Barnes. Observation of dipolar emission patterns from isolated Eu^{3+}:Y_2O_3 doped nanocrystals: new evidence for single ion luminescence. *Chemical Physics Letters*, Vol. 358, pp. 459–465, 2002.

[23] Y. V. Malyukin, A. A. Masalov, and P. N. Zhmurin. Single-ion fluorescence spec-

troscopy of a Y_2SiO_5:Pr^{3+} nanocluster. *Physics Letters A*, Vol. 316, pp. 147–152, 2003.

[24] R. Kolesov, K. Xia, R. Reuter, R. Stöhr, A. Zappe, J. Meijer, P. R. Hemmer, and J. Wrachtrup. Optical detection of a single rare-earth ion in a crystal. *Nature Communications*, Vol. 3, p. 1029, 2012.

[25] H. Goto, S. Nakamura, M. Kujiraoka, and K. Ichimura. Cavity-enhanced spectroscopy of a rare-earth-ion-doped crystal: observation of a power law for inhomogeneous broadening. *Optics express*, Vol. 21, pp. 24332–43, 2013.

[26] C. Yin, M. Rancic, G. G. de Boo, N. Stavrias, M. J. Sellars J. C. McCallum, and S. Rogge. Optical addressing of an individual erbium ion in silicon. *Nature*, Vol. 497, pp. 91–94, 2013.

[27] T. Utikal, E. Eichhammer, L. Petersen, A. Renn, S. Götzinger, and V. Sandoghdar. Spectroscopic detection and state preparation of a single praseodymium ion in a crystal. *Nature communications*, Vol. 5, p. 3627, 2014.

[28] R. M. Macfarlane and R. M. Shelby. *Spectroscopy of solids containing rare-earth ions*. North-Holland, 1987.

[29] 渡辺正. 元素大百科事典. 朝倉書店, 2007.

[30] D. Suter. *The physics of laser-atom interactions*. Cambridge University Press, 1997.

[31] H. H. Caspers, H. E. Rast, and R. A. Buchanan. Energy levels of Pr^{3+} in LaF_3. *The Journal of Chemical Physics*, Vol. 43, pp. 2124–2128, 1965.

[32] M. R. Brown, J. S. S. Whiting, and W. A. Shand. Ion—ion interactions in rare-earth-doped LaF_3. *The Journal of Chemical Physics*, Vol. 43, pp. 1–9, 1965.

[33] M. J. Weber. Spontaneous emission probabilities and quantum efficiencies for excited states of Pr^{3+} in LaF_3. *The Journal of Chemical Physics*, Vol. 48, pp. 4774–4780, 1968.

[34] E. Y. Wong, O. M. Stafsudd, and D. R. Johnston. Absorption and fluorescence spectra of several praseodymium-doped crystals and the change of covalence in the chemical bonds of the praseodymium ion. *The Journal of Chemical Physics*, Vol. 39, pp. 786–793, 1963.

[35] Y. C. Chen, K. Chiang, and S. R. Hartmann. Spectroscopic and relaxation character of the ${}^3P_0 - {}^3H_4$ transition in LaF_3:Pr^{3+} measured by photon echoes. *Physical Review B*, Vol. 21, pp. 40–47, 1980.

[36] I. Nakamura, T. Yoshihiro, H. Inagawa, S. Fujiyoshi, and M. Matsushita. Spectroscopy of single Pr^{3+} ion in LaF_3 crystal at 1.5 K. *Scientific Reports*, Vol. 4, p. 7364, 2014.

[37] B. Maximov and H. Schulz. Space group, crystal structure and twinning of lanthanum trifluoride. *Acta Crystallographica Section B Structural Science*, Vol. 41, pp. 88–91,

1985.

[38] A. Zalkin and D. H. Templeton. Refinement of the trigonal crystal structure of lanthanum trifluoride with neutron diffraction data. *Acta Crystallographica Section B Structural Science*, Vol. 41, pp. 91–93, 1985.

[39] R. Laiho and M. Lakkisto. Investigation of the refractive indices of LaF_3, CeF_3, PrF_3 and NdF_3. *Philosophical Magazine Part B*, Vol. 48, pp. 203–207, 1983.

[40] A. M. van Oijen, M. Ketelaars, J. Köhler, T. J. Aartsma, and J. Schmidt. Spectroscopy of single light-harvesting complexes from purple photosynthetic bacteria at 1.2 K. *The Journal of Physical Chemistry B*, Vol. 102, pp. 9363–9366, 1998.

[41] M. Fujiwara, S. Fujiyoshi, and M. Matsushita. Single-component reflecting objective for ultraviolet imaging and spectroscopy at cryogenic temperature. *Journal of the Optical Society of America B*, Vol. 26, pp. 1395–1399, 2009.

[42] S. Fujiyoshi, M. Hirano, M. Matsushita, M. Iseki, and M. Watanabe. Structural change of a cofactor binding site of flavoprotein detected by single-protein fluorescence spectroscopy at 1.5 K. *Physical Review Letters*, Vol. 106, p. 078101, 2011.

[43] M. Fujiwara, S. Fujiyoshi, and M. Matsushita. Single-component reflecting objective for low-temperature imaging and spectroscopy of single nano objects. *Physics Procedia*, Vol. 13, pp. 38–41, 2011.

[44] H. Inagawa, Y. Toratani, K. Motohashi, I. Nakamura, M. Matsushita, and S. Fujiyoshi. Reflecting microscope system with a 0.99 numerical aperture designed for three-dimensional fluorescence imaging of individual molecules at cryogenic temperatures. *in preparation*.

[45] E. F. Burton. Refractive indexes of helium I and II. *Nature*, Vol. 140, pp. 1015–1015, 1937.

[46] National Astronomical Observatory of Japan. *Rika nenpyo (Chronological scientific tables 2014)*. Maruzen Publishing, 2013.

[47] T. Hinohara, Y. I. Hamada, I. Nakamura, M. Matsushita, and S. Fujiyoshi. Mechanical stability of a microscope setup working at a few kelvins for single-molecule localization. *Chemical Physics*, Vol. 419, pp. 246–249, 2013.

[48] R. W. P. Drever, J. L. Hall, F. V. Kowalski, J. Hough, G. M. Ford, A. J. Munley, and H. Ward. Laser phase and frequency stabilization using an optical resonator. *Applied Physics B Photophysics and Laser Chemistry*, Vol. 31, pp. 97–105, 1983.

[49] R. Shelby, R. Macfarlane, and C. Yannoni. Optical measurement of spin-lattice relaxation of dilute nuclei: LaF_3:Pr^{3+}. *Physical Review B*, Vol. 21, pp. 5004–5011, 1980.

Acknowledgements

With this thesis, I conclude the seven-years lasting study of single RE ion doped in crystal. I thank many people for their kind advices and supports. At first, I would like to express the deepest appreciation to Assoc. prof. M. Matsushita, the supervisor of the study and the chief examiner of the graduation exam, for his long-standing tutelage. I also appreciate to the examiners, Prof. K. Asahi, Prof. Y. Okuda, Prof. M. Kozuma, Prof. em. A. Hosoya, and Prof. S. Murakami for their advices to improve the thesis.

I had been given a lot of technical supports and advices to carry out the difficult experiment. Pr^{3+}-doped LaF_3 crystals were borrowed by Prof. M. Masaharu (Kumamoto Univ.) and Prof. Y. Takahashi (Kyoto Univ.). Professor Kozuma gave me helpful advices about the ULE optical cavity. The aspherical reflecting objective, which is the indispensable component of the microscope, was manufactured by Sankyo Optics Industry. Without their excellent technique, the development of the objective has never been completed.

I was financially supported by the GCOE program on "Nano science and Quantum Physics" in Tokyo Institute of Technology. I would like to thank them for giving environment for a long going study.

I am deeply grateful to members of Matsushita laboratory and Minami laboratory in Tokyo Institute of Technology. Particularly, Dr. S. Fujiyoshi, the assistant professor of Matsushita Lab., mentored me heartily with everything day after day. Mr. H. Inagawa designed the aspheric reflecting objective. Development of the reflecting objectives is the essence of the single-molecule studies in Matsushita Lab. I feel so lucky to use the superior objective and to demonstrate its performance.

I owe my deepest gratitude to my family and friends inside and outside the university. Recalling a lot of names, finally I would like to call my parents Hiroya and Keiko. They have taken care of the high-maintenance son with their bounty up to now.